Filho MA, Pereira JM, Azenha M, Sena-Cruz J (2025) Environmental Boundary Conditions for Prediction of Temperature Distribution in Hybrid GFRP Sandwich Panels under Service Conditions. Journal of Composites for Construction, 29(5): 04025038. https://doi.org/10.1061/JCCOF2.CCENG-5159

Environmental boundary conditions for prediction of temperature distribution in hybrid GFRP sandwich panels under service conditions

Marco Abreu Filho [1], João Miguel Pereira [2], Miguel Azenha [3], José Sena-Cruz [4*]

[1] PhD Candidate, ISISE/ARISE, University of Minho, Department of Civil Engineering, 4800-058 Guimarães, Portugal, marcoabreufilho@civil.uminho.pt
[2] Assistant Researcher, ISISE/ARISE, University of Minho, Department of Civil Engineering, 4800-058 Guimarães, Portugal, jpereira@civil.uminho.pt
[3] Professor Associate with Habitation, ISISE/ARISE, University of Minho, Department of Civil Engineering, 4800-058 Guimarães, Portugal, miguel.azenha@civil.uminho.pt
[4] Professor Associate with Habitation, ISISE/ARISE, University of Minho, Department of Civil Engineering, 4800-058 Guimarães, Portugal, jose.sena-cruz@civil.uminho.pt
* Corresponding Author

ABSTRACT: Understanding and accurately predicting the thermal behaviour of fibre-reinforced polymer (FRP) composites is critical for their reliable application in structural systems. This study focuses on predicting temperature distributions within hybrid FRP sandwich panels composed of a pultruded glass fibre-reinforced polymer (GFRP) box, a closed-cell polyurethane foam core, and a steel fibre-reinforced self-compacting concrete (SFRSCC) topping layer. An extensive experimental programme was conducted under both controlled and external environmental conditions. The controlled phase involved thermal cycling and exposure to a high-pressure sodium (HPS) lamp to simulate radiant heating effects, while the outdoor phase captured real-world thermal fluctuations. Temperature was monitored using embedded PT100 sensors, and additional equipment was used to record ambient conditions, including solar radiation. Through meticulous experimental analyses and numerical simulations, this research evaluates the boundary conditions and thermal loads affecting the specimens, enabling the development and validation of numerical models. These models were designed to replicate transient heat transfer within the panels, accounting for convective heat exchange, direct and reflected radiation, and the influence of surface moisture during and after rainfall. The models achieved over 92% accuracy compared to experimental data, based on the mean absolute percentage error. Key findings show that disregarding reflected solar radiation from surrounding surfaces resulted in peak temperature underestimations of up to 13.9 °C, while neglecting evaporative cooling reduced the overall accuracy by approximately 6%. These results highlight the importance of calibrated numerical models for thermal analysis, ensuring the reliability of FRP-based structures under operational conditions. Furthermore, this research offers valuable insights for defining temperature distribution assessment methodologies regarding FRP composite structures in real-world applications.

Filho MA, Pereira JM, Azenha M, Sena-Cruz J (2025) Environmental Boundary Conditions for Prediction of Temperature Distribution in Hybrid GFRP Sandwich Panels under Service Conditions. Journal of Composites for Construction, 29(5): 04025038. https://doi.org/10.1061/JCCOF2.CCENG-5159

PRACTICAL APPLICATIONS: Predicting how temperature varies within fibre-reinforced polymer (FRP) sandwich panels is critical for ensuring their performance and durability in real-world structures, especially when exposed to environmental conditions. This study provides a practical approach to understanding and simulating the temperature distribution in FRP sandwich panels by combining experimental measurements with validated numerical models. The panels investigated include concrete-topped GFRP box structure with a foam core — a configuration relevant to bridge decks, façades, and floor systems. Field and laboratory tests were used to monitor how environmental factors such as solar radiation, surface moisture, and ambient temperature affect the heat transfer through the panels. The research demonstrated that commonly overlooked effects, such as reflected radiation from the ground or nearby surfaces, and evaporation during and after rain, can significantly impact surface temperatures and modelling accuracy. The methodology developed in this study provides a practical basis for engineers and designers to assess thermal behaviour under realistic service conditions. By identifying the environmental boundary conditions that influence the thermal response and should be considered, the results support more accurate design decisions and durability evaluations for composite structures in construction. This framework is adaptable and can be applied to future analyses involving similar materials or environments.

KEYWORDS: Fibre-Reinforced Polymer (FRP), Hybrid FRP sandwich panels; Thermal analysis; Numerical modelling; Environmental boundary conditions

INTRODUCTION

Fibre-reinforced polymers (FRP) materials are typically composed of two components, which are a combination of fibres and matrix. While the fibres act as the reinforcement, the matrix acts as the binder, maintaining and protecting the fibres (Moy 2013; Tang 2021). These materials boast a range of advantageous properties, including exceptional durability (Carra and Carvelli 2014), ease in-situ installation (Canning and Luke 2010; Chen et al. 2025), high strength-to-weight ratio (Alnahhal et al. 2006), corrosion resistance (Xin et al. 2016), and excellent fatigue resistance (Kumar et al. 2004). Consequently, FRP materials have garnered increasing attention within the construction sector (Bakis et al. 2001; Jurkiewiez et al. 2019).

FRP composites have thus found versatile applications within the construction industry, namely (i) as internal reinforcement of new and existing structures, (ii) in the strengthening and rehabilitation of reinforced concrete (RC) elements (e.g., externally bonded strengthening systems), (iii) all-composite structures, and (iv) hybrid

structures (Ahmed et al. 2020; Dushimimana et al. 2024). Hybrid systems generally promote synergies between the combined materials, thereby mitigating some of their inherent disadvantages (Ribeiro et al. 2024). The structural applications of FRP composites employ a variety of tensile components — including reinforcing bars (Ahmed et al. 2020), laminates (Dushimimana et al. 2024) and cables (Liu et al. 2015) — as well as bending components, such as profiles (Kossakowski and Wciślik 2022), cellular structures (Keller and Gürtler 2005), and sandwich panels (Kossakowski and Wciślik 2022), each adapted to specific structural demands. Sandwich panels, in particular, have gained prominence due to their high stiffness-to-weight ratio (Mastali et al. 2015), making them valuable components in modular and prefabricated systems (Sharafi et al. 2018; Liew et al. 2019). Such structures are ideal for applications like modular floors, bridge decks, and pier construction, where transport efficiency and robust structural performance are paramount (Garrido et al. 2015; Sharafi et al. 2018; Kim 2019; Kossakowski and Wciślik 2022). The integration of FRP materials into hybrid systems, which combine composites with traditional materials, such as concrete, or other materials, has shown remarkable benefits.

Despite the potential and benefits of FRP composites, several authors have highlighted over the years that the widespread adoption of these materials has been hampered by the lack of codes and design guidelines (Nystrom et al. 2003; Correia et al. 2010; Yang 2014; Gonilha et al. 2014; Kim 2019; Ali et al. 2021; Saleem et al. 2021; Lepretre et al. 2022; Qureshi 2022). To address this issue, significant research efforts have been dedicated to improving the understanding on the mechanical properties and structural behaviour of FRP composites in recent years (Shahrooz et al. 2007; Vizentin and Vukelic 2021). Moreover, there is enthusiasm for the potential boost in the adoption of FRP composites in Europe following the publication of the European Technical Specification CEN/TS 19101:2022 ‘Design of fibre-polymer composite structures’, in November 2022 (CEN - European Commitee for Standardization 2022).

This new standard represents a crucial moment, offering a framework for the design of composite structures. It represents a significant step forward in standardising design methodologies and ensuring the reliability of FRP-based structures. However, despite this progress, challenges remain, particularly with regards to understanding the response of FRP structures to environmental thermal actions and temperature variations (Shahrooz et al. 2007; Lepretre et al. 2022). In fact, the thermal performance and responses of FRP structures remain not fully investigated and understood (Lepretre et al. 2022). Consequently, their responses to thermal loads are often oversimplified (Shahrooz et al. 2007). Furthermore, the CEN WG4.T2 project team, responsible for developing the CEN/TS 19101:2022 (CEN - European Commitee for Standardization 2022), has recognised that this is an urgent issue in need of further attention from the scientific community.

FRP composites are known to exhibit mechanical properties with strong dependence on temperature; therefore, minor temperature fluctuations (far below the glass transition temperature, T_g) lead to changes in their physical properties (Stankiewicz 2017); environmental thermal conditions, whether daily fluctuations, seasonal changes or annual variations, pose dynamic challenges to structures, affecting their static and dynamic behaviour (Xia et al. 2013; 2017); non-uniform temperature distribution leads to thermal stresses within the structure, with temperature fluctuations at times exceeding operational loads on their impact at structural deformations (Xia et al. 2013; 2017; Zhou et al. 2017).

Previous experimental investigations have confirmed the significant impact of thermal variations on the structural behaviour of FRP systems. Mandal and Ray (2015) evaluated the flexural performance of a GFRP bridge deck subjected to both constant and gradient temperature fields, observing that thermally induced deflections (up to 5.17 mm) surpassed those generated by vehicular loading (2.99 mm). Similarly, Xi et al. (2004), through long-term field monitoring of GFRP decks in a bridge in Denver, United States, reported that thermal stresses routinely exceeded the strains produced by mechanical loads—even in winter—and, during summer, were over three times higher than those induced by service traffic. These findings underline the critical role that temperature plays in driving the deformation and stress patterns in fibre composite structures.

In addition, Tuwair et al. (2016) investigated the effects of thermal cycles on GFRP sandwich panels filled with polyurethane foam and exposed to freeze-thaw and high-temperature cycles, with temperatures ranging from -20°C to 50°C. A 24% reduction in ultimate flexural strength was reported after environmental conditioning. Although a marginal increase in stiffness was observed, tensile strength decreased by approximately 6%, indicating that prolonged exposure to thermal fluctuations—even within realistic environmental temperature ranges—can compromise the structural integrity and reliability of FRP systems. These studies collectively emphasize the necessity of considering environmental temperature effects not only during the design phase but also for long-term performance assessments.

However, despite the findings reported in earlier studies, limited research has addressed the internal temperature distribution within FRP sandwich structures under environmental thermal loads, particularly using embedded sensors for experimental validation. This study contributes to filling this gap by combining experimental measurements and numerical modelling to characterize the thermal gradients across a multilayered hybrid GFRP system.

Given the complex thermomechanical behaviour of FRP composites and the variability in their geometry and constituent materials, existing standards lack specificity for conducting structural thermal analyses (Lekou and

Philippidis 2008; Lepretre et al. 2022). However, understanding and accurately predicting the temperature distributions expected in critical scenarios is paramount at the design stage. These predictions are intrinsically tied to understanding the diverse boundary conditions affecting the structure, including accurate consideration regarding the impacts of radiation, convection and conduction (Miller and Weaver 2003).

The primary objective of this study is to develop and enhance numerical models using a finite element analysis software to investigate the behaviour of FRP sandwich structure panels consisting of glass-FRP (GFRP) face sheets/webs and a polyurethane foam (PUR) core, complemented by a top layer of steel fibre reinforced self-compacting concrete (SFRSCC) under serviceability climatic conditions. These models enable accurate depiction of the temperature distribution within the structural element in response to environmental thermal loads, considering the influences of radiation, convection and conduction. This research includes a comprehensive examination of the boundary conditions and a detailed record of the climatic events during the experimental campaign affecting the structural element under investigation. The validation of these models involves a meticulous analysis of the experimental results, focusing on the thermal analysis of the hybrid FRP sandwich panels.

This article presents an initial experimental campaign conducted in a controlled environment, followed by a subsequent campaign in an external setting, aimed at investigating and providing insights into the thermal distribution behaviour within the specimens under varying environmental conditions. A comprehensive analysis of the boundary conditions, with particular emphasis on the external environment, is subsequently performed. The experimental results are then systematically compared with the developed numerical models to evaluate the thermal response of hybrid GFRP sandwich structures subjected to environmental thermal loads under service conditions.

This study aims to contribute to a broader understanding of temperature behaviour in multilayer composite systems by presenting a structured and transferable methodology for thermal analysis under serviceability conditions. By combining experimentally validated parameters, realistic environmental data, and detailed modelling of boundary conditions, the proposed approach provides a solid framework that can be adapted to other applications involving similar materials and service environments. Furthermore, it supports the development of reliable thermal simulations for structural composites and offers a strong foundation for future studies aiming to extend this methodology to a wider range of configurations.

EXPERIMENTAL CAMPAIGN

This section provides a comprehensive overview of the specimens under investigation, followed by a detailed description of the experimental campaigns carried out during this study. Likewise, it details an initial experimental campaign carried out under controlled climatic conditions and, lastly, the process of monitoring the temperature within the panels under external environmental conditions.

Specimens

This research involved investigating the temperature distribution within two specimens consisting of a GFRP sandwich panel with an infill material, topped with a layer of steel fibre-reinforced self-compacting concrete (SFRSCC), as illustrated in Fig. 1a. Each specimen measured 1.5 meters in span and 30 cm in width, featuring a GFRP "box" part (face sheets and web) with a thickness of 6 mm, fabricated through pultrusion, and a closed-cell polyurethane foam core with a density of 60 kg/m^3. The pultrusion process involved simultaneously introducing the PUR foam blocks—already cut to the final panel dimensions— along with the resin impregnated glass-fibre reinforcement into the heated die. The laminate architecture included alternating layers of unidirectional roving, woven fabrics, and chopped strand mats to ensure both in-plane and through-thickness reinforcement. An unsaturated polyester resin served as the matrix for the GFRP and also ensured bonding between the fibre-reinforced laminate and the foam core. An epoxy adhesive was used during the casting of the freshly poured SFRSCC to enhance adhesion between the GFRP and the SFRSCC layer. Six PT100 Resistance Temperature Detector (RTD) sensors of Platinum 385, model NB-PTCO-002, were inserted into the specimens after manufacturing them. For this purpose, 2 mm-diameter holes were drilled at the intended sensor positions: the holes through the GFRP face sheets were made using a standard steel drill bit, while the foam core was drilled using a stainless steel welding rod, which offered the necessary rigidity to maintain hole alignment up to the 71 mm in depth. A predrilled wooden alignment plate was used to further ensure correct placement. The thermocouples were fixed in place by pouring a thermoset resin—polyester for the holes in the GFRP and polyurethane for the holes in the PUR core—with properties similar to the surrounding materials, in order to ensure consistency and to minimize discontinuities in the thermal and physical properties of the composite caused by the sensor installation. The sensors were positioned at the midpoint of the specimen length and along the central axis of the cross-section, as depicted in Fig. 1b. These panels were developed as part of a research project entitled 'Easyfloor-Development of Composite Sandwich Panels for Building Floor Rehabilitation'. For detailed

information regarding their design, manufacturing process, mechanical characterization, structural, fire and functional performance, refer to (Silva et al. 2022; Proença et al. 2024).

Controlled environment tests

Prior to subjecting the specimens to external climatic conditions, an initial experimental campaign was carried out using a walk-in climatic chamber, with dimensions of 2400 mm (length) × 1800 mm (width) × 2000 mm (height), temperature range between -25±1 ºC and +80±1 º C and relative humidity range between 30±2 % and 98±2 %. This initial campaign involved monitoring the temperature distribution within the specimens under different controlled conditions, carried out in different phases, as follows.

In the first phase (Phase I), equilibrium was initially established at 20 °C. The temperature was then gradually reduced at a rate of 0.076 °C/min until it reached -15 °C. This was followed by an heating phase at the same rate until the temperature reached 40 °C (this ramp took 12 hours); then, a subsequent cooling phase back to -15 °C over another 12 hours. This 24-hour thermal cycle (from -15 °C to 40 °C and back to -15 °C) was repeated ten times (see Fig. 2a). During this phase, both specimens were positioned inside the chamber in order to maximise the open space around their sides, as shown in Fig. 3a.

In a second phase (Phase II), the temperature was set at 20 °C and maintained for the entire period. The specimens were then exposed to a 1000 W high-pressure sodium (HPS) lamp, which emits a UV to IR spectrum, for 12 hours, followed by 12 hours without exposure to the lamp, completing a 24-hour cycle. This pattern was repeated over five times (see Fig. 2b). To ensure optimal exposure to the lamp, only one specimen was placed in the centre of the chamber with the lamp positioned 50 cm above it, as shown in Fig. 3b.

Concluding the initial experimental campaign, Phase III combined elements from Phases I and II. The specimen was subjected to temperature cycles from -15 °C to 40 °C, while simultaneously being exposed to the HPS lamp for 12 hours, followed by 12 hours without the lamp exposure, completing a 24-hour cycle. This sequence was repeated for 10 cycles (see Fig. 2c). Activation of the lamp was synchronised with an increase in temperature, and deactivation coincided with a decrease in temperature. The experimental configuration was the same as that used in Phase II (Fig. 3b).

The thermal cycles were designed to progressively calibrate the numerical model under increasingly complex thermal conditions prior to environmental exposure. The temperature range from −15 °C to 40 °C reflects realistic service conditions and was constrained by the operational limits of the high-pressure sodium lamp used for radiative heating. This protocol was developed to induce representative thermal gradients across the specimens,

enabling accurate evaluation of the model performance. The number of cycles adopted in each phase was defined based on the stability and consistency of sensor readings, supporting confidence in the calibration process.

The temperature throughout of the mid-span cross section of the specimens was monitored using six PT100 sensors, as illustrated in Fig. 1b. Additionally, two PT100 RTD Platinum 385 sensors were strategically positioned within the climatic chamber to enhance temperature tracking. The data from these sensors were utilized in the developed numerical models (see Section *NUMERICAL MODELS*). Data acquisition was carried out using a DataTaker (Thermo Fisher Scientific 2011), recording two measurements per minute.

Fig. 2 also highlights key points of interest to be further analysed (see Section *Controlled environment tests* in *RESULTS AND DISCUSSION*). For Phases I (Fig. 2a) and III (Fig. 2c), these points include: i) the midpoint between the 10th negative peak and the preceding positive peak (Halfway Through Cooling - HWC); ii) the 10th negative peak (NP); iii) the midpoint between the 10th negative peak and the 10th positive peak (Halfway Through Heating - HWH); and iv) the 10th positive peak (PP). For Phase II (Fig. 2b), the points of interest are: i) half an hour after the lamp exposure begins in the third cycle; ii) six hours of lamp exposure during the third cycle; and iii) the midpoint between the end of lamp exposure in the third cycle and the specimen's return to thermal equilibrium at 20 °C (Halfway Through Cooling - HWC).

Outdoor environment tests

Following the initial experimental campaign, the specimens were subjected to outdoor testing (the experimental setup is shown in Fig. 4) under the environmental conditions of the city of Guimarães in Portugal, more specifically, located at coordinates 41°45'32''N and 8°29'06''W. This testing spanned a duration of ten days, from 9 October 2023 at 9:24 AM to 19 October 2023 at 9:24 AM (local time). The specimens were positioned at the monitoring location five days prior to the start of monitoring. This deliberate pre-exposure period facilitated gradual adaptation to the environmental climatic nuances prevalent in the region, thereby minimizing the potential impact of sudden environmental shifts encountered upon transitioning the specimens from a controlled indoor condition to the dynamic outdoor environment.

The data acquisition was performed using a DataTaker, with a frequency of 2 acquisitions per minute. The temperature within the specimens was monitored by the six TP100 sensors as referred in Fig. 1b. Additionally, the air shade temperature was recorded using an additional Platinum 385 PT100 RTD sensor, which was adequately shielded to prevent interference from the solar radiation. Solar radiation data was collected using a silicon pyranometer (Kipp & Zonen B.V. 2018) positioned approximately 5 meters from the experimental setup (see Fig.

4). This placement was chosen to minimise potential shading from nearby objects or human activity, such as during routine data retrieval from the acquisition system.

The specimens were also positioned to prevent any shadowing from adjacent objects. One lateral face (Face A) of the specimen was perpendicularly aligned at an azimuth angle of 55°NE, while the opposite face (Face B) was perpendicularly oriented to 55°SW.

NUMERICAL MODELS

As mentioned before, a finite element software (DIANA 2023) was used to build numerical models able to replicate the non-linear transient heat transfer phenomena within the specimens under investigation. The first goal was to closely emulate the experimentally measured temperature distributions within the specimens, considering both the controlled environment in the climatic chamber and the external environmental conditions to which they were subjected in the city of Guimarães, Portugal, and subsequently evaluate their reliability.

For the numerical analysis under controlled climatic conditions, a 3D model was used to account for the non-uniform incidence of the lamp on the specimens. The model was meshed with twenty-node isoparametric hexahedral elements (CHX20H). Taking advantage of the central axis of symmetry, half of the cross-section and longitudinal length were modelled (see Fig. 5), with element dimensions of 5 mm × 5 mm × 10 mm (width × height × length). The elements were deliberately elongated to reduce computational processing time. This elongation was perpendicular to the main temperature gradients, thus having minimal impact on the results.

The temperature data obtained from the climatic chamber was incorporated into the model as a convective boundary condition, applied uniformly throughout the peripheral region, excluding the axis of symmetry. The lamp's irradiation pattern was modelled using a Gaussian distribution, characterized by a peak heat flux of 595 W/m² at the centre. This intensity, assessed using the pyranometer, decreases symmetrically from the centre following a Gaussian profile (Equation 1) and reaches near-zero at a radial distance of 40 cm from the focal point, thereby defining the spatial extent of the irradiation. The lamp's radiation was incorporated into the model as a heat flow boundary condition, exclusively impacting the top surface of the model.

$$f(x) = 595 \cdot e^{-\frac{x^2}{2 \cdot 0.067^2}} \quad (1)$$

In the context of the numerical analysis under external climatic conditions, a 2D model was employed and meshed using eight-node quadrilateral isoparametric elements (CQ8HT) based on quadratic interpolation and Gauss

integration. To account for varying solar exposure on each face, a complete cross-section was modelled (see Fig. 6), with element dimensions of 5 mm × 5 mm (width × height).

The air shade temperature, measured by the external PT100 sensor, was incorporated into the model as a convective boundary condition, applied uniformly throughout the model's peripheral region. The remaining factors incorporated into this numerical model (e.g., solar radiation) are discussed in detail in the following sub-sections. The material properties used in the model are summarised in Table 1. The GFRP properties were collected from the characterization made in (Silva et al. 2022; Proença et al. 2024), while the properties for the other materials were estimated based on literature (Nagy et al. 2015; Zhang et al. 2017; Asadi et al. 2018; Lepretre et al. 2022). The values extracted from the literature were verified and calibrated by means of the comprehensive initial experimental campaign involving the specimens in the controlled environment (climatic chamber), as detailed in Section

Controlled environment tests in *EXPERIMENTAL CAMPAIGN*, prior to conducting the outdoor tests.

Furthermore, the thermal properties were considered constant throughout the simulations. This simplification was adopted based on the fact that the study focuses on serviceability conditions, with temperature ranges remaining within moderate limits. Within this range, variations in thermal properties are expected to be limited, and their potential influence on the heat transfer behaviour is considered minor.

Convective heat transfer and emissivity

In addition to the thermal properties, aspects including the heat transfer coefficient and materials' emissivity must also be addressed when conducting transient heat transfer analyses. The standard EN 1991-1-2 (CEN - European Commitee for Standardization 1991) suggests a range of 9 $W \cdot m^{-2} \cdot °C^{-1}$ to 25 $W \cdot m^{-2} \cdot °C^{-1}$ for the convective heat transfer coefficient in concrete, with 25 $W \cdot m^{-2} \cdot °C^{-1}$ being appropriate for fire-exposed materials. Lee et al. (2009) reported experimental research indicating that for wind speeds between 2 and 3 m/s, the coefficient for concrete falls within 14 $W \cdot m^{-2} \cdot °C^{-1}$ to 15 $W \cdot m^{-2} \cdot °C^{-1}$. For the sake of simplicity, in this study a value of 15 $W \cdot m^{-2} \cdot °C^{-1}$ was adopted for the concrete's convective heat transfer coefficient, since the exact wind speed on-site was not measured, although some wind presence in the test location was expected. This is further supported by data from the nearest meteorological station to the test site, according to data obtained in ("Historical Weather Data for Guimarães | Visual Crossing" n.d.), which recorded wind speeds predominantly corresponding to grade 2 on the Beaufort scale (1.6–3.3 m/s (Penwarden 1973)) during the test period. There were only occasional instances of

lower wind speeds, classified as grade 0 or 1 (0.0–1.5 m/s (Penwarden 1973)), and higher speeds of grade 3 (3.4–5.4 m/s (Penwarden 1973)). Occurrences of winds exceeding grade 3 were minimal and considered negligible. Typically, numerical models in the literature assign a heat transfer coefficient of 25 $W \cdot m^{-2} \cdot °C^{-1}$ for GFRP materials (Keller et al. 2006; Morgado et al. 2018; Zhang et al. 2021), particularly when dealing with exposure to fire. However, when considering GFRP under environmental serviceability conditions, including solar radiation, the relevant literature is scarce. Nevertheless, a value of 21 $W \cdot m^{-2} \cdot °C^{-1}$ has previously been used for such scenarios (Lepretre et al. 2022), which this study has also adopted. This higher heat transfer coefficient for the GFRP layer is supported by findings from the initial experimental campaign, which demonstrated that the GFRP layer exhibits a higher heat transfer rate with the environment compared to the SFRSCC layer (see Section *Controlled environment* tests in *RESULTS AND DISCUSSION*).

In terms of emissivity, the value for concrete usually ranges from 0.85 to 0.95 (Tayşi and Abid 2015). For this study, the concrete emissivity was defined as a constant, adopting the average value of 0.9. Regarding GFRP, researchers such as Morgado et al. (2018) and Keller et al. (2006), in their numerical modelling studies, defined an emissivity that varies linearly from 0.75 to 0.95 between temperatures of 20 °C and 1000 °C. However, employing a fixed value of 0.75 is also acceptable (Morgado et al. 2018), particularly considering that the specimen under investigation will remain within the serviceability temperature range.

In summary, the heat transfer coefficients for SFRSCC and GFRP were set at 15 $W \cdot m^{-2} \cdot °C^{-1}$ and 21 $W \cdot m^{-2} \cdot °C^{-1}$, with emissivity values of 0.90 and 0.75, respectively. It is important to note that the climatic chamber provided nearly constant forced convection over the specimens. During the initial experimental campaign, as detailed in Section *Controlled environment* tests in *EXPERIMENTAL CAMPAIGN*, the chamber's circulation fans were continuously operational, ensuring consistent air movement within the chamber. In phase I (Fig. 2a) and phase III (Fig. 2c), where no temperature plateaus were present, the climate chamber continuously adjusted the temperature, either increasing or decreasing it as needed. In phase II (Fig. 2b), despite a defined temperature plateau, the HPS lamp produced constant heat during its operation. Even after deactivation, the lamp required time to cool down, leading to prolonged operation of the chamber's circulation fans to stabilize the temperature and maintain it nearly constant. As a result, in simulations involving controlled climatic conditions, the heat transfer coefficients were set to 30 $W \cdot m^{-2} \cdot °C^{-1}$ for SFRSCC and 40 $W \cdot m^{-2} \cdot °C^{-1}$ for GFRP, respectively.

Thermal actions

Within this section, the approach to evaluate and account for the additional boundary conditions and thermal loads influencing the specimens in the external environment is detailed. The model integrated global solar radiation data obtained from the pyranometer as a heat flow boundary condition, applied at the upper surface. Additionally, the model encompassed diffuse solar radiation, solar radiation on lateral surfaces and solar radiation reflected by the ground as additional heat flow boundary conditions, which are detailed in the following subsections. In summary, the models addressed the interaction of the thermal conduction, convection and radiation phenomena.

Solar radiation

The global solar radiation, as measured by the pyranometer (I_{global}), is presented in Fig. 7, alongside with the diffuse solar radiation (I_{diffuse}) estimated based on the model proposed by Bortolini et al. (Bortolini et al. 2013) where the diffuse fraction (k_d) is determined by Equation 2.

$$k_d = \frac{I_{\text{diffuse}}}{I_{\text{global}}} = 0.9888 + 0.3950k_t - 3.7003{k_t}^2 + 2.2905{k_t}^3 \quad (2)$$

Equation 2 denotes I_{diffuse} as the diffuse solar radiation (in W/m^2), I_{global} as the global radiation (in W/m^2) recorded by the pyranometer (Duffie and Beckman 2013) and k_t is the clearness index, which is determined based on Equation 3 (Kalogirou 2009; Duffie and Beckman 2013).

$$k_t = \frac{I_{\text{global}}}{G_{\text{oH}}} \quad (3)$$

Equation 3 denotes G_{oH} as the average daily extraterrestrial solar radiation (in W/m^2) reaching the top of the atmosphere on a specific day of the year, referred as d, which can be calculated analytically by using Equation 4 (Kalogirou 2009).

$$G_{\text{oH}} = G_{\text{sc}}\left[1 + 0.033\cos\left(\frac{360d}{365}\right)\right][\cos(\phi)\cos(\delta)\cos(h) + \sin(\phi)\sin(\delta)] \quad (4)$$

In Equation 4, G_{sc} represents the solar constant, established as 1366.1 W/m^2 (Gueymard 2004). The ϕ denotes for the location's latitude, δ stands for the solar declination angle, calculated for specific day of the year (d) according to Equation 5 (Shivalingaswamy and Kagali 2011; Abood 2015), and h refers to the hour angle. This last parameter

was obtained from a Solar Position Algorithm (SPA) ("Solar Position Algorithm (SPA)" n.d.) developed by the US National Renewable Energy Laboratory.

$$\delta = 23.45\sin\left[\frac{360}{365}(284 + d)\right] \quad (5)$$

After accounting for the diffuse solar radiation, the next step involved calculating the direct solar radiation on the lateral surfaces (webs) of the specimens ($I_{Inclined}$). This included the surface orientated 55° north-east (Face A – see Fig. 4) as well as the surface orientated 55° south-west (Face B), using equation 6 (Herrería-Alonso et al. 2020).

$$I_{Inclined} = I_{\text{horizontal}} \times \cos(\theta_i) \quad (6)$$

In Equation 6, $I_{\text{horizontal}}$ denotes the global solar radiation on a horizontal surface (in W/m^2), as recorded by the pyranometer (Duffie and Beckman 2013), while θ_i represents the angle of solar incidence on the inclined surface, which can be calculated using Equation 7 (Kalogirou 2009; Herrería-Alonso et al. 2020).

$$\begin{aligned}\cos(\theta_i) = {} & \sin(\phi)\sin(\delta)\cos(\beta) - \cos(\phi)\sin(\delta)\sin(\beta)\cos(\theta_s) \\ & + \cos(\phi)\cos(\delta)\cos(h)\cos(\beta) + \sin(\phi)\cos(\delta)\cos(h)\sin(\beta)\cos(\theta_s) \\ & + \cos(\delta)\sin(h)\sin(\beta)\sin(\theta_s)\end{aligned} \quad (7)$$

In Equation 7, ϕ denotes the latitude of the location, δ stands for the solar declination angle calculated for a given day of the year (d) using Equation 5 (Shivalingaswamy and Kagali 2011; Abood 2015), β represents the inclination angle of the surface with respect to the horizontal, θ_s stands for the azimuth angle of the surface, i.e. the angle between the normal to the surface from true south (with westward designated as positive), and h refers to the hour angle, a parameter obtained from the SPA ("Solar Position Algorithm (SPA)" n.d.).

According to Kalogirou (2009), when considering vertical surfaces (β = 90°), Equation 8 can be applied as a simplified form of Equation 7.

$$\begin{aligned}\cos(\theta_i) = {} & -\cos(\phi)\sin(\delta)\cos(\theta_s) + \sin(\phi)\cos(\delta)\cos(h)\cos(\theta_s) \\ & +\cos(\delta)\sin(h)\sin(\theta_s)\end{aligned} \quad (8)$$

Fig. 8 depicts the solar radiation affecting the lateral faces of the test specimens, as calculated for the period covered by this study.

Ground reflection irradiation

Given the proximity of the specimens to the ground surface (30 cm), it was necessary to consider the solar radiation reflected by the ground. It is worth noting, however, that reflected radiation can also arise from surrounding built elements, such as retaining walls, pavements, or nearby structural components — a condition commonly observed in bridge decks and façade systems. As such, this factor may be relevant in a broader range of service environments. According to Muneer et al. (2004), this reflected component can be significant, particularly at northern latitudes due to the sun's low elevation angles. Although ground reflectance varies throughout the day – with morning albedo values generally lower than those in the afternoon (Enriquez et al. 2012) – Ineichen et al. (1987) and Ineichen et al. (1990) suggest that using a constant ground reflectance yields satisfactory results, indicating limited benefits from employing an anisotropic ground reflectance model. Therefore, the component reflected by the ground can be estimated with a simplified approach based on the global solar irradiation (Muneer et al. 2004), as indicated in Equation 9 (Psiloglou et al. 1997; Enriquez et al. 2012; Yousef et al. 2023).

$$G_r = \rho_g I_{\text{global}} \frac{1 - \cos\ \beta}{2} \tag{9}$$

In Equation 9, G_r represents the ground-reflected irradiance (in W/m^2), ρ_g denotes the mean ground albedo, I_{global} is the global solar irradiation (in W/m^2), β and is the inclination angle of the surface.

As can be seen in Fig. 4, the specimens were placed on a pavement consisting of pre-moulded concrete blocks. According to Kotak et al. (2015), typical albedo values for a concrete surface range from 0.25 to 0.7. Sanjuán et al. (2021) conducted a study assessing the albedo of various precast concrete pavements and obtained values ranging from 0.13 to 0.79. For this study, an approximate average value of 0.48 was adopted for a dry surface. Chiodetti et al. (2016) explored the impact of rain on concrete albedo on different locations, determining that wet concrete exhibits an albedo approximately 45% lower than dry concrete. Consequently, during precipitation periods (see Section *Air shade temperature and rainfall*), the albedo was decreased by 45%. Fig. 9 depicts the radiation reflected by the ground, as calculated for the bottom surface and both lateral faces of the test specimen. Note that when the direct solar radiation on a given lateral face was zero, the radiation reflected by the ground was also set to zero, since the face was expected to be in the shade. Furthermore, to streamline the analytical approach, the ground drying process was assumed to be linear, along with the increase in albedo once the rain ceased and the ground returned to a dry state (see Fig. 10).

Air shade temperature and rainfall

Fig. 10 presents the air shade temperature data recorded by the external PT100 temperature sensor. This figure also delineates the monitoring periods coinciding with rainfall events and the periods after the rain during which the specimens were still in a wet or damp state.

In October 12, 2023, at approximately 15:00 (experimental time t = 77 hours), sporadic rainfall occurred, persisting until October 13 at 22:00 (experimental time t = 108.5 hours), resulting in a cumulative precipitation of about 8 mm. After rainfall, a thorough examination via visual and tactile methodologies indicated sustained dampness on the specimen's surface through the following day. Visual assessment revealed subtle sheen and slight material darkening, while tactile examination corroborated these observations by detecting residual moisture. The specimen was considered fully dry on the surface again on October 14, 2023, around 20:00 (experimental time t = 130.5 hours), upon the absence of aforementioned indicators.

A subsequent period of discontinuous rainfall commenced on October 15, 2023, around 15:00 (experimental time t = 150 hours), persisting until October 16, 2023, around 22:00 (experimental time t = 180.5 hours), with a total precipitation of approximately 11 mm. Subsequently, from October 17, 2023, around 4:30 am (experimental time t = 187 hours), a more intense and sustained rainfall ensued, persisting until the conclusion of the experiment on October 19, 2023, at 9:24 am (experimental time t = 240 hours), accumulating approximately 135 mm of rainfall. Notably, following the onset of the second rainy period, the specimens did not return to a dry state before the conclusion of the experiment. The data regarding rainfall measurements (in mm), was obtained from ("Weather Archive Guimarães - Meteoblue" n.d.).

In the context of experimental investigations into temperature distribution within structures exposed to environmental conditions, a significant consideration arises with the occurrence of precipitation, namely rainfall. As stated above, the specimens underwent periods of rain exposure throughout the monitoring period. According to Mehrabian and Samadi (2010), a wet surface presents higher heat transfer coefficients compared to a dry surface. Corroborating this observation, Williams (1963) indicates that this variation in heat transfer can be correlated with the difference between the wet surface temperature and the surrounding air temperature. Moreover, Cui et al. (2019) describe in their study a simplified methodology for quantifying this increase in heat transfer coefficients, denoted as evaporative heat transfer coefficients (h_e) component, which can be estimated according to Equation 10.

$$\frac{h_e}{h_c} = \frac{r}{R_{\text{Water}}\,\rho c_{\text{p}} Le^{\frac{2}{3}}(T_{\text{w}} - T_{\text{a}})}\left(\frac{P_{\text{w}}}{T_{\text{w}}} - \frac{P_{\text{a}}}{T_{\text{a}}}\right) \quad (10)$$

In Equation 10, h_c represents convective heat transfer, r denotes the latent heat of water (in kJ/kg), which is calculated using Equation 11; R_{Water} stands for the gas constant for water vapor (461.5 J/kg·K), ρ is the density of water (997 kg/m³), c_{p} denotes the specific heat of water (4.19 kJ/kg·K), and Le represents the Lewins number, typically set to 0.857 when water vapor diffuses through air (Cui et al. 2019); T_{w} is the surface temperature, T_{a} denotes the air shade temperature, P_{w} represents the water vapor partial pressure on the surface, and P_{a} is the water vapor partial pressure in ambient air. For consistency with the methodology outlined by Cui et al. (2019), temperatures in Equations 10 to 13 are expressed in Kelvin. Additionally, the water vapor partial pressure can be determined using Equation 12.

$$r = 2497.848 - 2.324T_a \quad (11)$$

$$P_{(w,\,a)} = \varphi p_s \quad (12)$$

In Equation 12, φ represents the relative humidity, and p_s denotes the saturated vapor pressure (in Pa), which can be calculated using Equation 13, where T represents the measured temperature.

$$p_s = 3385.5\exp\left[-8.093 + 0.936(T + 42.61)^{1/2}\right] \quad (13)$$

Fig. 11 shows the variation in the evaporative heat transfer coefficient, as calculated according to Equation 10. These values were subsequently combined with the convective heat transfer coefficient. In order to simplify the h_e calculation, it was considered that the specimen's natural drying process followed a linear progression.

RESULTS AND DISCUSSION

In this section, the numerical results are presented and compared with the experimental results. Following this, a detailed analysis of the key observations from both the initial experimental campaign conducted in the climatic chamber and the subsequent external environment campaign will be presented, focusing on specific factors influencing the final outcomes.

Controlled environment tests

In analysing the initial experimental campaign, this section begins with a summary of the main results from Phases I (Fig. 2a) and II (Fig. 2b), followed by a more detailed examination of Phase III (Fig. 2c). For Phases I and II, Fig. 12 illustrates thermal profiles obtained from the sensors within the specimens at key points, together with

numerical results. Specifically, Phase I thermal profiles depict: i) the 10th negative peak (NP); ii) the midpoint between the 10th negative peak and the 10th positive peak (Halfway Through Heating - HWH); iii) the midpoint between the 10th negative peak and the preceding positive peak (Halfway Through Cooling - HWC) and iv) the 10th positive peak (PP) (see also Fig. 2a). Meanwhile, Phase II thermal profiles correspond to measurements taken: i) at the midpoint between the cessation of lamp exposure in the third cycle and the specimen's return to thermal equilibrium at 20 °C (Halfway Through Cooling - HWC); ii) half an hour after the lamp exposure begins during the third cycle and iii) six hours of lamp exposure in the third cycle (see also Fig. 2b).

During Phase I, the cyclic temperature pattern applied, without plateaus, resulted in varying maximum and minimum temperatures recorded by the different sensors (Fig. 12a). Sensor S1 showed a maximum temperature of around 37.3 °C and a minimum of about -12.5 °C throughout the process. Sensor S6 recorded a maximum temperature of approximately 39.4 °C and a minimum of roughly -15 °C, closely matching the temperature of the climatic chamber. Positioned at the innermost part of the specimen (in the centre of the foam), Sensor S4 registered a maximum temperature of about 35.6 °C and a minimum of approximately -11.5 °C during this phase. The sensors located in the outermost layers (Sensor S1 and Sensor S6) clearly indicated that the SFRSCC layer exhibited a lower heat transfer rate with the surroundings compared to GFRP. Additionally, it is important to mention that the temperature distribution patterns remained remarkably consistent across all cycles applied. This analysis provided valuable insights into heat exchange between the test specimens and the environment, as well as within the specimens themselves. Furthermore, it's worth noting that the experimental data collected from both specimens yielded consistent results between them.

In the sequence, as observed in the Phase II thermal profiles (Fig. 12b), the upper sensors, which were closer to the lamp, displayed a more pronounced influence as expected. This influence progressively diminished with the depth of the sensors inside the specimen. Notably, sensor S6, the furthest from the lamp, showed no noticeable impact, maintaining a temperature nearly identical to that of the climate chamber. For instance, sensor S1 reached a maximum temperature of 35.5 °C due to exposure to the lamp, while sensor S4, positioned more centrally within the foam core, reached a maximum temperature of approximately 24.2 °C. During this phase of the experiment, the specimen exhibited a temperature gradient of 15.5 °C across its cross-section. Additionally, the numerical simulation showed considerable accuracy compared to the experimental results for most of the sensors. During this phase, sensor S4 emerged as the most critical point for the instants analysed (largest error). However, the disparity observed between the numerical and experimental results did not exceed 4.9%, corresponding to an approximate temperature discrepancy of 1.1 °C.

Fig. 13 presents the detailed experimental and numerical results for sensors S1, S4, and S6 during Phase III (last phase of the controlled environmental tests). These sensors correspond to the outermost sensor at the top of the specimen in the SFRSCC layer, the innermost sensor in the foam core, and the outermost sensor at the bottom face sheet of the specimen, respectively. Additionally, Fig. 13d illustrates the thermal profiles at four specific time points: t = 218 hours, t = 224 hours, t = 230 hours, and t = 236 hours. These times represent, respectively, the midpoint between the 10th negative peak and the preceding positive peak (Halfway Through Cooling - HWC), the 10th negative peak (NP), the midpoint between the 10th negative peak and the 10th positive peak (Halfway Through Heating - HWH), and the 10th positive peak (PP) (see also Fig. 2c).

The figures above depict the temperature fluctuations within the test specimen, influenced by the cyclical thermal loads and exposure to the HPS lamp. During this phase, sensor S1 reached a peak temperature of around 52.7 °C, exceeding the set temperature of the climate chamber by 12.7 °C, with a minimum of around -12.6 °C. In contrast, sensor S6 recorded a maximum of around 39.5 °C and a minimum of -14.9 °C, closely mirroring the conditions of the climate chamber. Sensor S4, located in the innermost position, showed a maximum temperature of around 39.7 °C and a minimum of approximately -11 °C. Notably, its minimum temperature was similar to the Phase I results, while the maximum was slightly higher (around 4 °C), indicating a subtle influence of the lamp on this sensor. Positioned between the SFRSCC layer and the GFRP top face sheet, sensor S2 recorded a maximum temperature at the GFRP as approximately 52.2 °C. The maximum temperature gradient in the cross-section of the specimen during this phase was approximately 14.5 °C.

The numerical simulation closely aligned with the experimental results across all phases under controlled climatic conditions, validating the accuracy of the developed models. Furthermore, as shown in the region highlighted in Fig. 13b, a small discrepancy was observed for sensor S4. This deviation occurred primarily during the transition from the cooling phase to the heating phase; however, the average difference between the numerical and experimental curves remained below 0.5 °C, with a maximum pointwise difference of 0.72 °C. This level of agreement is within acceptable bounds for transient thermal modelling of multilayer composite systems considering the temperature range imposed during this phase, and the low level of discrepancy further reinforces the robustness of the numerical predictions. Additional information and details regarding the initial experimental campaign are also available in (Abreu Filho et al. 2024).

Outdoor environment tests

After validating the numerical models and material properties through the initial experimental campaign, this subsection presents the results obtained under external environmental conditions. Fig. 14 shows the experimental data collected from the two specimens, each instrumented with six PT100 sensors arranged, as illustrated in Fig. 1b. The corresponding numerical results are also included for comparison.

As illustrated in Fig. 14a, Sensor S1 recorded peak temperatures of around 49.8 °C and 50.3 °C for specimens 1 and 2, respectively, whereas the numerical simulation had output a peak of 50.3 °C, closely mirroring the experimental results. In contrast, the minimum temperatures recorded on specimens 1 and 2, which occurred at the third lowest temperature peak (experimental time, t = 68 hours), were 9.6 °C and 9.7 °C, respectively, while the numerical simulation recorded a minimum temperature of 11.7 °C, representing the most significant disparity observed between the experimental and numerical results throughout the monitoring period, with a deviation of approximately 2 °C. The second largest deviation occurred at the second lowest temperature peak (experimental time, t = 44 hours), with recorded temperatures of approximately 10.7 °C and 10.8 °C for specimens 1 and 2, respectively, compared to a simulated temperature of 11.9 °C, reflecting a difference of around 1.2 °C between the experimental and numerical results.

The observed disparity in the lowest peaks between the numerical and experimental results may be explained by wind speed fluctuations, leading to variations in the convective heat transfer coefficient (Emmel et al. 2007; Evangelisti et al. 2017). These variations are expected to have a more pronounced effect on the most exposed horizontal surface (Mirsadeghi et al. 2013), particularly the upper surface of the specimen. This assumption is supported by the observation that the differences in the negative peaks are evident in Sensors S1, S2 and S3 (Fig. 14a, b and c), while they appear imperceptible in Sensors S4, S5 and S6 (Fig. 14d, e and f). However, it is important to note that, as outlined in Section *NUMERICAL MODELS*, no wind speed measurements were taken in the field, and a fixed value was used for the convective heat transfer coefficient.

Nevertheless, it is noteworthy that despite these differences in the lower peaks, the Mean Absolute Percentage Error (MAPE) calculated between the average of the experimental curves and the numerical curve for Sensor S1 was 5.63%, indicating a numerical model accuracy exceeding 94% for Sensor S1.

Sensor S4 (Fig. 14c) is also worthy of a more in-depth analysis. It recorded a peak temperature of 40.9 °C for specimen 1 and 42.1 °C for specimen 2, contrasting with the numerical model's peak temperature of 42.5 °C. At the lower end, this sensor registered 12.7 °C for specimen 1 and 14.3 °C for specimen 2, whereas the numerical

model registered the lowest temperature of 12.5 °C. Notably, this sensor exhibited the most significant disparities between the experimental findings of specimens 1 and 2. This variation could stem from potential mismatches in sensor positioning during installation, indicating a slight misalignment (either upwards or downwards) compared to the other sensors, as they benefited from clearer positioning references, such as material borderlines. Being positioned the centre of the foam, sensor S4 lacked a distinct reference point, possibly resulting in less accurate positioning. In addition, this sensor also recorded the highest MAPE calculated between the average curve of the experimental results and the numerical outcomes. However, it stood at 7.22%, suggesting that the numerical model has generally maintained an overall accuracy of over 92%.

Moreover, sensors S2, S3, S5 and S6 (Fig. 14b, c, e, and f) also underwent the MAPE calculation for the average curve between the experimental values in contrast to the numerical results, resulting in values of 5.71%, 5.89%, 5.97% and 6.53%, respectively. This emphasises the level of accuracy achieved by the numerical models compared to the experimental results.

Upon closely examining sensor S6, the effects of solar radiation reflected by the ground, as discussed in Section *Ground reflection irradiation*, become evident. As shown in Fig. 14a, sensor S6 recorded peak temperatures of 42.4 °C for specimen 1 and 41.9 °C for specimen 2, approximately 10.1 °C higher than the air shade temperature (around 32.1 °C) observed during the monitoring period. The numerical simulations, which incorporate the ground-reflected solar radiation, resulted in a peak temperature of 41.6 °C at this sensor. In contrast, an additional analysis indicated that disregarding the solar radiation reflected by the ground would result in a peak temperature of 28.3 °C at sensor S6—about 3.8 °C below the air shade temperature and approximately 13.9 °C lower than the experimental measurements. This highlights the critical importance of considering a structure's surroundings when setting boundary conditions for numerical models aimed at investigating temperature distributions under serviceability conditions.

Furthermore, during this study, it was evident that accounting for the evaporative heat transfer coefficient (see Section *Air shade temperature and rainfall*) during rainy periods and post-rain dampness results in closer alignment with the experimental data. In general, rainfall occurrences and the accounting of the evaporative heat transfer coefficient (h_e) had the effect of minimising the minimum and maximum temperatures. This led to a tendency towards bringing the temperature measured on the test specimen closer to the air shade temperature.

Focussing solely on rainy periods and the moments in which the specimen remained wet or damp afterward—thus including the total period in which h_e was considered—the average overall calculated MAPE was around 6.16% between the numerical results and the average of the experimental results. On the other hand, further

analysis has shown that ignoring h_e raised the average overall MAPE to 12.04% for the same period. These results underscore the importance of considering precipitation events and accounting for the evaporative heat transfer coefficient in the numerical simulations to achieve closer agreement with experimental observations.

Finally, Fig. 15 illustrates the thermal profiles at four specific moments of interest: t = 5.8 hours, t = 44 hours, t = 130 hours, and t = 219 hours. These time instants correspond, respectively, to the first positive peak, the second lowest temperature peak, the moment when the specimen is assumed to have returned to a dry state after the first rainy period and the final positive peak during a rainy period.

Fig. 15 demonstrates the congruence between the experimental and the numerical thermal profiles across diverse stages of the monitoring period, encompassing varying climatic conditions. This observation substantiates the precision attainable through the numerical modelling approach.

INVESTIGATIONS INTO CRITICAL SCENARIOS

Considering the capabilities of the numerical models presented in the previous section in predicting real environmental conditions, these models offer a promising approach to investigate the complexities of the temperature distribution within the specimens. Once calibrated and validated, they can be effectively employed to investigate critical scenarios, offering insights into how temperature gradients are manifested within the specimens under severe climatic conditions which they might experience. Therefore, this section investigates and discusses the temperature distribution within the specimens during the most severe environmental conditions in Guimarães, Portugal, over the past ten years.

During the last decade, between 2013 and 2023, the city of Guimarães in Portugal experienced its most severe weather events (within this decade) during the week spanning from 5th August 2016 to 11th August 2016 for the highest temperatures, and from 5th January 2021 to 11th January 2021 for the lowest temperatures. Fig. 16 illustrates the air shade temperatures for these weeks based on data obtained from (“Historical Weather Data for Guimarães | Visual Crossing” n.d.).

The global solar radiation for the aforementioned weeks, as depicted in Fig. 17, was estimated by using a mathematical model for solar radiation developed by Van Breugel and Koenders (2001). This model was employed considering an hourly clearness index estimated from climatic parameters obtained in (“Historical Weather Data for Guimarães | Visual Crossing” n.d.). The diffuse solar radiation was calculated using the model proposed by Bortolini et al. (2013), outlined in Equation 2. In addition, the radiation on each face of the specimen was calculated according to Equation 6 and Equation 8.

Finally, the solar radiation reflected by the ground, encompassing the bottom and lateral faces of the specimens, as depicted in Fig. 18, was calculated using Equation 9 as elaborated in the Section *Ground reflection irradiation*. Fig. 19a shows the thermal distribution within the specimen during the most severe heatwave recorded in the city of Guimarães in the last decade (from 2013 to 2023), which occurred between 5th August 2016 and 11th August 2016. In contrast, Fig. 19b illustrates the specimen's thermal distribution during the coldest week recorded in Guimarães during the same period, taking place between 5th January 2021 and 11th January 2021.

Fig. 19 indicates that, during the most severe conditions of the past decade in Guimarães, the specimen would attain a maximum temperature of 69.1 °C in the SFRSCC layer, with the GFRP structure reaching a peak of 68.68 °C. Moreover, the structure would exhibit a thermal gradient exceeding 33 °C. In contrast, the minimum temperature would register at -1.1 °C in the GFRP structure, while the SFRSCC layer would experience a minimum temperature of -0.9 °C. During the most severe case of minimum temperature, the thermal gradient would be only 1.3 °C.

Shifting focus to the applicable standards, the EN 1991-1-5 (CEN - European Commitee for Standardization 2003), which is currently in force in Europe, provides principles and guidelines for the thermal action assessment of various structures, including buildings, bridges and their components. Although this standard does not include specific guidelines regarding FRP composites, it is still pertinent to conduct comparative assessments. Considering a structure in Portugal, the most severe scenario for high temperatures involves bridge decks. Notably, type 1 decks (steel decks) are the most critical in this context, and the maximum temperature for these decks can be calculated using a simplified equation provided by the national annex of this standard, as outlined in Equation 14.

$$T_{e,max} = T_{max} + 15\ °C \tag{14}$$

In the Equation 14, $T_{e,max}$ signifies the maximum temperature (°C) of an exposed surface, while T_{max} denotes the maximum air shade temperature (°C), established according to the Portuguese national annex for the corresponding zone. In the case of Guimarães, this parameter is fixed at 40 °C.

In turn, the minimum temperature for the same type of structure (steel bridge deck) would be obtained through Equation 15.

$$T_{e,min} = T_{min} - 10\ °C \tag{15}$$

Equation 15 defines $T_{e,min}$ as the minimum temperature of an exposed surface (°C), with T_{min} representing the minimum air shade temperature (°C), specified by the Portuguese national annex for the respective zone. For Guimarães, this value is standardized at -5 °C.

According to the EN 1991-1-5 (CEN - European Commitee for Standardization 2003), the worst-case scenario would predict a maximum temperature of 55 °C for a structure in Guimarães, Portugal. However, the numerical analysis revealed that, in the most severe case of the last decade, the specimen under study would reach a maximum temperature of 69.1 °C, exceeding the standard's worst-case prediction by 14.1 °C. With regard to minimum temperatures, the worst-case scenario given by EN 1991-1-5 (CEN - European Commitee for Standardization 2003) would result in a minimum temperature of -15 °C. Nonetheless, measurements from the past ten years indicated a minimum temperature of -1.1 °C.

Furthermore, still according to the Portuguese National Annex of the EN 1991-1-5 (CEN - European Commitee for Standardization 2003) standard, the worst-case scenario for thermal gradients in Portugal also applies to type 1 bridge decks, where the maximum thermal gradient is expected to reach 18 °C. In contrast, numerical models indicated that the hybrid GFRP structure under study would have experienced a thermal gradient exceeding 33 °C under the most severe conditions of the past 10 years. This represents a difference of more than 15 °C between the worst-case scenario predicted by the standard and the gradient calculated in this study for the structure under investigation.

In terms of design, it is critical to properly estimate the service temperatures of FRP composite structures, particularly as CEN/TS 19101:2022 (CEN - European Commitee for Standardization 2022) outlines specific temperature considerations for these systems. The standard provides provisions to account the temperature effects (temperature conversion factor) under service conditions, for material temperatures in members, joints, and components, between -40 °C and T_g - 20 °C, where T_g represents the glass transition temperature of the composite materials. Therefore, the temperature conversion factor accounts for changes in material properties (stiffness and strength) resulting from service temperatures differing from 20 °C. This underscores the importance of calibrated numerical models capable of accurately simulating and predicting service temperatures in composite structures. Notably, even the most extreme scenarios provided by the Portuguese National Annex from EN 1991-1-5 (CEN - European Commitee for Standardization 2003) would lead to non-conservative predictions of potential maximum temperatures and thermal gradients if applied to the hybrid GFRP composite structure under study.

It is important to emphasise that the EN 1991-1-5 (CEN - European Commitee for Standardization 2003) does not include specific provisions for FRP composites, thus its applicability to the present case study is not fully covered.

The type 1 deck discussed refers to steel decks (steel box girder, steel truss or plate girder). As expected, the unique thermal properties of the hybrid panel components will result in different thermal responses. In locations such as Guimarães, where the minimum air shade temperature is unlikely to fall below -5°C, the observed differences in minimum temperatures (between the simplified equation from the EN 1991-1-5 and the temperatures observed during the most severe case of the last decade, as obtained by the numerical models) may not significantly impact decision-making processes. However, a disparity of more than 14 °C in the case of the maximum temperatures would hold substantial significance within this context.

Moreover, in line with the guidelines of CEN/TS 19101:2022 (CEN - European Commitee for Standardization 2022), this study highlights the importance of conducting targeted investigations when dealing with FRP composite structures exposed to environmental thermal conditions. Such investigations are essential to accurately determine the maximum and minimum temperatures, as well as the thermal gradients that these structures may encounter under serviceability conditions.

CONCLUSIONS

This study investigated the temperature distribution in hybrid GFRP sandwich panels under serviceability conditions, combining experiments conducted in controlled environments and under outdoor exposure. In addition to analysing the thermal behaviour of the composite system, particular emphasis was placed on evaluating the environmental boundary conditions that influence heat transfer in such structures. Based on the results obtained, the following main conclusions can be drawn:

- The results obtained from both specimens were consistent, indicating good reproducibility across materials and sensors. Nonetheless, minor variations were observed in the sensor positioned at the centre of the foam core, likely due to the difficulty of accurately installing this particular sensor, which may have resulted in slight misalignment.
- The SFRSCC layer exhibited a lower rate of heat exchange with the surrounding environment compared to the GFRP.
- The numerical simulations exhibited strong agreement with the experimental results, achieving an accuracy exceeding 92%, thus validating the models. This performance is primarily attributed to the meticulous evaluation of the environmental boundary conditions, despite being based on a simplified monitoring setup composed only of temperature sensors and a pyranometer.

- In addition to the fundamental boundary conditions, two factors significantly influenced the model's accuracy: (i) ground-reflected solar radiation, which increased the bottom surface temperature by up to 13 °C despite the absence of direct solar exposure; and (ii) the evaporative heat transfer coefficient during and after rainfall. Integrating this latter factor enhanced the model's accuracy by over 5% during wet or damp periods. However, this coefficient tended to align the surface temperature with the surrounding air temperature and thus played a limited role in exploring the maximum and minimum temperatures within the structure. Nonetheless, it proved essential for representing transient thermal responses associated with precipitation and should be considered in similar modelling efforts, particularly in studies focused on thermal or energy efficiency and short-term climatic effects.
- Simulations conducted under historical extreme weather conditions in Guimarães indicated that surface temperatures could have reached up to 69.1 °C, revealing a 14.1 °C deficit relative to the 55 °C value for the worst-case maximum temperature scenario defined in EN 1991-1-5 (type 1 bridge decks), according to the Portuguese national annex. It is crucial to underscore the absence of established guidelines for predicting temperatures in FRP composite materials. Attempting to adapt simplified formulations, even those corresponding to the most severe scenarios outlined in current standards, may lead to underestimation of thermal loads and significant design errors if applied to FRP systems.

Building on these results, calibrated numerical models based on finite element methods serve as essential tools for predicting temperatures in FRP composite structures. The importance of investigating temperature distributions is reinforced by CEN/TS 19101:2022, which provides a temperature conversion factor, considering changes in material properties due to temperatures deviating from 20 °C under serviceability conditions. Therefore, assessing the temperature distribution in composite structures remains of paramount importance as part of the design phase. While the results demonstrate a high level of consistency and accuracy, some limitations must be acknowledged. The reduced number of specimens (two) restricts statistical generalisation, and certain environmental factors—such as relative humidity and wind speed—were not directly measured during the outdoor phase, although they were considered through indirect estimations and modelling assumptions. Additionally, whereas the numerical model was carefully calibrated and validated with experimental data, further studies are encouraged to explore its applicability to other FRP sandwich configurations. Nevertheless, the modelling strategies adopted in this study have shown promising potential for supporting the thermal analysis and design of composite systems under realistic environmental conditions.

ACKNOWLEDGMENTS

This work was partly financed by FCT / MCTES through national funds (PIDDAC) under the R&D Unit Institute for Sustainability and Innovation in Structural Engineering (ISISE), under reference UID/04029/Institute for Sustainability and Innovation in Structural Engineering (ISISE), and under the Associate Laboratory Advanced Production and Intelligent Systems ARISE under reference LA/P/0112/2020. The first author would also like to acknowledge the doctoral grant 2022.13310.BD, awarded by the Fundação para a Ciência e a Tecnologia (FCT), and co-financed by the European Social Fund and national funds through FCT/MCTES. Acknowledgments are also extended to LEST – Laboratório de Estruturas, for their technical and material support.

DATA AVAILABILITY STATEMENT

Some or all data, models, or code that support the findings of this study are available from the corresponding author upon reasonable request.

NOTATION

c_p: specific heat of water (kJ/kg·K)

d: day number in the year (-)

G_{oH}: average daily extraterrestrial solar radiation (W/m^2)

G_r: ground-reflected irradiance (W/m^2)

G_{sc}: solar constant (W/m^2)

h: hour angle (º)

h_c: convective heat transfer (W/m^2·ºC)

h_e: evaporative heat transfer coefficient (W/m^2·ºC)

$I_{diffuse}$: diffuse solar radiation (W/m^2)

I_{global}: global solar radiation (W/m^2)

$I_{horizontal}$: global solar radiation on a horizontal surface (W/m^2)

$I_{Inclined}$: solar radiation on an inclined surface (W/m^2)

k_d: diffuse fraction (-)

k_t: clearness index (-)

Le: Lewins number (-)

723 P_a: water vapor partial pressure in ambient air (Pa)

724 P_w: water vapor partial pressure on the surface (Pa)

725 p_s: saturated vapor pressure (Pa)

726 R_{Water}: gas constant for water vapor (J/kg·K)

727 r: latent heat of water (kJ/kg)

728 T: Temperature (ºC)

729 T_a: air temperature (K)

730 T_w: surface temperature (K)

731 t: time (h)

732 β: inclination angle of a surface with respect to the horizontal (º)

733 δ: declination angle (º)

734 θ_i: angle of solar incidence on the inclined surface (º)

735 θ_s: azimuth angle of a surface (º)

736 ϕ: location's latitude (º)

737 φ: relative humidity (%)

738 ρ: density (kg/m³)

739 ρ_g: mean ground albedo (-)

740

741 **REFERENCES**

742 Abood, Akram Abdulameer. 2015. “A Comprehensive Solar Angles Simulation and Calculation Using Matlab.”
743 *International Journal of Energy and Environment* 6 (4): 367–76.

744 Abreu Filho, Marco, João M. Pereira, Miguel Azenha, and José Sena-Cruz. 2024. “Experimental and Numerical
745 Analyses on the Thermal Distribution within Hybrid FRP Sandwich Panels under Different Climatic
746 Conditions.” In *Proceedings of the 21st European Conference on Composite Materials - Volume 3 -*
747 *Material and Structural Behavior – Simulation & Testing*, 976–83. Nantes. https://doi.org/10.60691/yj56-
748 np80.

Ahmed, Azzam, Shuaicheng Guo, Zuhua Zhang, Caijun Shi, and Deju Zhu. 2020. "A Review on Durability of Fiber Reinforced Polymer (FRP) Bars Reinforced Seawater Sea Sand Concrete." *Construction and Building Materials*. Elsevier Ltd. https://doi.org/10.1016/j.conbuildmat.2020.119484.

Ali, Hafiz Tauqeer, Roya Akrami, Sakineh Fotouhi, Mahdi Bodaghi, Milad Saeedifar, Mohammad Yusuf, and Mohamad Fotouhi. 2021. "Fiber Reinforced Polymer Composites in Bridge Industry." *Structures* 30 (April):774–85. https://doi.org/10.1016/j.istruc.2020.12.092.

Alnahhal, Wael I, Methee; Chiewanichakorn, Amjad J Aref, and Sreenivas Alampalli. 2006. "Temporal Thermal Behavior and Damage Simulations of FRP Deck." *Journal of Bridge Engineering* 11 (4): 452–64. https://doi.org/10.1061/ASCE1084-0702200611:4452.

Asadi, Iman, Payam Shafigh, Zahiruddin Fitri Bin Abu Hassan, and Norhayati Binti Mahyuddin. 2018. "Thermal Conductivity of Concrete – A Review." *Journal of Building Engineering*. Elsevier Ltd. https://doi.org/10.1016/j.jobe.2018.07.002.

Bakis, C E, L C Bank, V L Brown, E Cosenza, J F Davalos, J J Lesko, A Machida, S H Rizkalla, and T C Triantafillou. 2001. "Fiber-Reinforced Polymer Composites for Construction-State-of-the-Art Review." *Journal of Composites for Construction* 6 (2): 73–87. https://doi.org/10.1061/ASCE1090-026820026:273.

Bortolini, Marco, Mauro Gamberi, Alessandro Graziani, Riccardo Manzini, and Cristina Mora. 2013. "Multi-Location Model for the Estimation of the Horizontal Daily Diffuse Fraction of Solar Radiation in Europe." *Energy Conversion and Management* 67:208–16. https://doi.org/10.1016/j.enconman.2012.11.008.

Breugel, K Van, and E A B Koenders. 2001. "Solar Radiation - Effect on Solar Radiation on the Risk of Cracking in Young Concrete." Delft.

Canning, Lee, and Sam Luke. 2010. "Development of FRP Bridges in the UK –An Overview." *Advances in Structural Engineering* 13 (5): 823–35.

Carra, Guglielmo, and Valter Carvelli. 2014. "Ageing of Pultruded Glass Fibre Reinforced Polymer Composites Exposed to Combined Environmental Agents." *Composite Structures* 108 (1): 1019–26. https://doi.org/10.1016/j.compstruct.2013.10.042.

CEN - European Commitee for Standardization. 1991. "EN 1991-1-2: Eurocode 1: Actions on Structures - Part 1-2: General Actions - Actions on Structures Exposed to Fire."

776 CEN - European Commitee for Standardization. 2003. “EN 1991-1-5: Eurocode 1: Actions on Structures - Part
777 1-5: General Actions - Thermal Actions.” Brussels.

778 CEN - European Commitee for Standardization. 2022. “TS 19901: Design of Fibre-Polymer Composite
779 Structures.”

780 Chen, Guipeng, Yanlei Wang, and Shutong Yang. 2025. “Elliptical FRP–Concrete–Steel Double-Skin Tubular
781 Columns under Cyclic Compression: Fundamental Characteristics and Modeling.” *Engineering Structures*
782 326 (March). https://doi.org/10.1016/j.engstruct.2024.119517.

783 Chiodetti, Matthieu, Amy Lindsay, Patrick Dupeyrat, Didier Binesti, Eric Lutun, Khalid Radouane, and Sophie
784 Mousel. 2016. “PV Bifacial Yield Simulation with a Variable Albedo Model.” In *32nd European*
785 *Photovoltaic Solar Energy Conference and Exhibition*. Munich.

786 Correia, Joao R., Fernando Branco, José Gonilha, Nuno Silva, and Dinar Camotim. 2010. “Glass Fibre
787 Reinforced Polymer Pultruded Flexural Members: Assessment of Existing Design Methods.” *Structural*
788 *Engineering International: Journal of the International Association for Bridge and Structural Engineering*
789 *(IABSE)* 20 (4): 362–69. https://doi.org/10.2749/101686610793557771.

790 Cui, Yaping, Jingchao Xie, Jiaping Liu, and Peng Xue. 2019. “Experimental and Theoretical Study on the Heat
791 Transfer Coefficients of Building External Surfaces in the Tropical Island Region.” *Applied Sciences*
792 *(Switzerland)* 9 (6). https://doi.org/10.3390/app9061063.

793 DIANA. 2023. *DIANA User’s Manual - Release 10.8*.

794 Duffie, John A., and William A. Beckman. 2013. *Solar Engineering of Thermal Processes*. Wiley.

795 Dushimimana, Aloys, Anastasios P. Vassilopoulos, José Sena-Cruz, João M. Pereira, Luís Correia, Susana
796 Cabral-Fonseca, and Ricardo Cruz. 2024. “Behavior of CFRP Composites and Epoxy Adhesives after
797 Long-Term Exposure to Outdoor and Laboratory-Controlled Environments.” *Construction and Building*
798 *Materials* 438 (August). https://doi.org/10.1016/j.conbuildmat.2024.137201.

799 Emmel, Marcelo G., Marc O. Abadie, and Nathan Mendes. 2007. “New External Convective Heat Transfer
800 Coefficient Correlations for Isolated Low-Rise Buildings.” *Energy and Buildings* 39 (3): 335–42.
801 https://doi.org/10.1016/j.enbuild.2006.08.001.

802 Enriquez, R., L. Zarzalejo, M. J. Jiménez, and M. R. Heras. 2012. "Ground Reflectance Estimation by Means of
803 Horizontal and Vertical Radiation Measurements." *Solar Energy* 86 (11): 3216–26.
804 https://doi.org/10.1016/j.solener.2012.07.020.

805 Evangelisti, L., C. Guattari, P. Gori, and F. Bianchi. 2017. "Heat Transfer Study of External Convective and
806 Radiative Coefficients for Building Applications." *Energy and Buildings* 151 (September):429–38.
807 https://doi.org/10.1016/j.enbuild.2017.07.004.

808 Garrido, Mário, João R. Correia, Thomas Keller, and Fernando A. Branco. 2015. "Adhesively Bonded
809 Connections between Composite Sandwich Floor Panels for Building Rehabilitation." *Composite*
810 *Structures* 134 (December):255–68. https://doi.org/10.1016/j.compstruct.2015.08.080.

811 Gonilha, José A., João R. Correia, and Fernando A. Branco. 2014. "Structural Behaviour of a GFRP-Concrete
812 Hybrid Footbridge Prototype: Experimental Tests and Numerical and Analytical Simulations."
813 *Engineering Structures* 60 (February):11–22. https://doi.org/10.1016/j.engstruct.2013.12.018.

814 Gueymard, Christian A. 2004. "The Sun's Total and Spectral Irradiance for Solar Energy Applications and Solar
815 Radiation Models." *Solar Energy* 76 (4): 423–53. https://doi.org/10.1016/j.solener.2003.08.039.

816 Herrería-Alonso, Sergio, Andrés Suárez-González, Miguel Rodríguez-Pérez, Raúl F. Rodríguez-Rubio, and
817 Cándido López-García. 2020. "A Solar Altitude Angle Model for Efficient Solar Energy Predictions."
818 *Sensors (Switzerland)* 20 (5). https://doi.org/10.3390/s20051391.

819 "Historical Weather Data for Guimarães | Visual Crossing." n.d. Accessed June 3, 2024.
820 https://www.visualcrossing.com/weather-history/guimar%C3%A3es/.

821 Ineichen, Pierre, Olivier Guisan, and Richard Perez. 1990. "Ground-Reflected Radiation and Albedo." *Solar*
822 *Energy* 44 (4): 207–14. https://doi.org/doi:10.1016/0038-092x(90)90149-7.

823 Ineichen, Pierre, Richard Perez, and Robert Seals. 1987. "The Importance of Correct Albedo Determination for
824 Adequately Modeling Energy Received by Tilted Surfaces." *Solar Energy* 39 (4): 301–5.
825 https://doi.org/doi:10.1016/s0038-092x(87)80016-6.

826 Jurkiewiez, Bruno, Alaa Koaik, and Sylvain Bel. 2019. "Static Behaviour up to Failure of a Full-Scale GFRP-
827 Concrete Hybrid Footbridge." *Engineering Structures* 199 (November).
828 https://doi.org/10.1016/j.engstruct.2019.109629.

Kalogirou, Soteris A. 2009. "Environmental Characteristics." In *Solar Energy Engineering*, 49–762. Elsevier. https://doi.org/10.1016/b978-0-12-374501-9.00002-9.

Keller, Thomas, and Herbert Gürtler. 2005. "Quasi-Static and Fatigue Performance of a Cellular FRP Bridge Deck Adhesively Bonded to Steel Girders." *Composite Structures* 70 (4): 484–96. https://doi.org/10.1016/j.compstruct.2004.09.028.

Keller, Thomas, Craig Tracy, and Aixi Zhou. 2006. "Structural Response of Liquid-Cooled GFRP Slabs Subjected to Fire - Part I: Material and Post-Fire Modeling." *Composites Part A: Applied Science and Manufacturing* 37 (9): 1286–95. https://doi.org/10.1016/j.compositesa.2005.08.006.

Keller, Thomas, Craig Tracy, and Aixi Zhou. 2006. "Structural Response of Liquid-Cooled GFRP Slabs Subjected to Fire - Part II: Thermo-Chemical and Thermo-Mechanical Modeling." *Composites Part A: Applied Science and Manufacturing* 37 (9): 1296–1308. https://doi.org/10.1016/j.compositesa.2005.08.007.

Kim, Yail J. 2019. "State of the Practice of FRP Composites in Highway Bridges." *Engineering Structures* 179 (January):1–8. https://doi.org/10.1016/j.engstruct.2018.10.067.

Kipp & Zonen B.V. 2018. "Instruction Sheet SP Lite2 Silicon Pyranometer." www.kippzonen.com.

Kossakowski, Paweł Grzegorz, and Wiktor Wciślik. 2022. "Fiber-Reinforced Polymer Composites in the Construction of Bridges: Opportunities, Problems and Challenges." *Fibers* 10 (4). https://doi.org/10.3390/fib10040037.

Kotak, Y, M S Gul, T Muneer, and SM Ivanova. 2015. "Investigating the Impact of Ground Albedo on the Performance of PV Systems." In *CIBSE Technical Symposium*, 16–17. London.

Kumar, Prakash, K. Chandrashekhara, and Antonio Nanni. 2004. "Structural Performance of a FRP Bridge Deck." *Construction and Building Materials* 18 (1): 35–47. https://doi.org/10.1016/S0950-0618(03)00036-9.

Lee, Yun, Myoung Sung Choi, Seong Tae Yi, and Jin Keun Kim. 2009. "Experimental Study on the Convective Heat Transfer Coefficient of Early-Age Concrete." *Cement and Concrete Composites* 31 (1): 60–71. https://doi.org/10.1016/j.cemconcomp.2008.09.009.

Lekou, D. J., and T. P. Philippidis. 2008. "Mechanical Property Variability in FRP Laminates and Its Effect on Failure Prediction." *Composites Part B: Engineering* 39 (7–8): 1247–56. https://doi.org/10.1016/j.compositesb.2008.01.004.

Lepretre, Emilie, Philippe Jandin, Nihal El Bourkadi, Samuel Durand, and Jean François Caron. 2022. "Design Approach for FRP Structures: A Focus on Thermal Design." In *10th International Conference on FRP Composites in Civil Engineering. CICE 2021. Lecture Notes in Civil Engineering*, 198 LNCE:2446–57. Springer Science and Business Media Deutschland GmbH. https://doi.org/10.1007/978-3-030-88166-5_212.

Liew, J. Y.R., Y. S. Chua, and Z. Dai. 2019. "Steel Concrete Composite Systems for Modular Construction of High-Rise Buildings." *Structures* 21 (October):135–49. https://doi.org/10.1016/j.istruc.2019.02.010.

Liu, Yue, Bernd Zwingmann, and Mike Schlaich. 2015. "Carbon Fiber Reinforced Polymer for Cable Structures—A Review." *Polymers*. MDPI AG. https://doi.org/10.3390/polym7101501.

Mandal, Bibekananda, and Chaitali Ray. 2015. "Bending of FRP Bridge Deck under the Combined Effect of Thermal and Vehicle Load." *Advances in Structural Engineering: Materials, Volume Three*, January, 2493–2503. https://doi.org/10.1007/978-81-322-2187-6_191.

Mastali, M., I. B. Valente, Joaquim A.O. Barros, and Delfina M.F. Gonçalves. 2015. "Development of Innovative Hybrid Sandwich Panel Slabs: Experimental Results." *Composite Structures* 133 (December):476–98. https://doi.org/10.1016/j.compstruct.2015.07.114.

Mehrabian, M. A., and B. Samadi. 2010. "Heat-Transfer Characteristics of Wet Heat Exchangers in Parallel-Flow and Counter-Flow Arrangements." *International Journal of Low-Carbon Technologies* 5 (4): 256–63. https://doi.org/10.1093/ijlct/ctq032.

Miller, J R, and P M Weaver. 2003. "Temperature Profiles in Composite Plates Subject to Time-Dependent Complex Boundary Conditions." *Composite Structures* 59:267–78. www.elsevier.com/locate/compstruct.

Mirsadeghi, M., D. Cóstola, B. Blocken, and J. L.M. Hensen. 2013. "Review of External Convective Heat Transfer Coefficient Models in Building Energy Simulation Programs: Implementation and Uncertainty." *Applied Thermal Engineering*. https://doi.org/10.1016/j.applthermaleng.2013.03.003.

Morgado, T., N. Silvestre, J. R. Correia, F. A. Branco, and T. Keller. 2018. "Numerical Modelling of the Thermal Response of Pultruded GFRP Tubular Profiles Subjected to Fire." *Composites Part B: Engineering* 137 (March):202–16. https://doi.org/10.1016/j.compositesb.2017.11.009.

Moy, Stuart. 2013. "Advanced Fiber-Reinforced Polymer (FRP) Composites for Civil Engineering Applications." In *Developments in Fiber-Reinforced Polymer (FRP) Composites for Civil Engineering*, 177–204. Elsevier Inc. https://doi.org/10.1533/9780857098955.2.177.

Muneer, T., C. Gueymard, and H. Kambezidis. 2004. "Daily Irradiation." *Solar Radiation and Daylight Models*, January, 35–59. https://doi.org/10.1016/B978-075065974-1/50010-3.

Muneer, T., C. Gueymard, and H. Kambezidis. 2004. "Ground Albedo." *Solar Radiation and Daylight Models*, January, 303–16. https://doi.org/10.1016/B978-075065974-1/50014-0.

Nagy, Balázs, Salem Georges Nehme, and Dóra Szagri. 2015. "Thermal Properties and Modeling of Fiber Reinforced Concretes." In *Energy Procedia*, 78:2742–47. Elsevier Ltd. https://doi.org/10.1016/j.egypro.2015.11.616.

Nystrom, Halvard E, Steve E Watkins, Antonio Nanni, M Asce, and Susan Murray. 2003. "Financial Viability of Fiber-Reinforced Polymer (FRP) Bridges." *Journal of Management in Engineering* 19 (1): 2–8. https://doi.org/10.1061/ASCE0742-597X200319:12.

Penwarden, A D. 1973. "Acceptable Wind Speeds in Towns." *Building Science* 8 (3): 259–67. https://doi.org/https://doi.org/10.1016/0007-3628(73)90008-X.

Proença, M., M. Garrido, J. R. Correia, and J. Sena-Cruz. 2024. "Experimental Study on the Fire Resistance of All-Composite and Hybrid Web-Core Sandwich Panels for Building Floors." *Composite Structures* 337 (June). https://doi.org/10.1016/j.compstruct.2024.118071.

Proença, Miguel, Pedro Santos, Luís Godinho, Albano Neves e Sousa, João R. Correia, Mário Garrido, and José Sena-Cruz. 2024. "Acoustic Behaviour of GFRP-PUR Web-Core Composite Sandwich Panels." *Construction and Building Materials* 438. https://doi.org/10.1016/j.conbuildmat.2024.137195.

Psiloglou, B. E., C. A. Balaras, M. Santamouris, and D. N. Asimakopoulos. 1997. "Calculation of Ground Albedo for the Estimation of Global Radiation on Tilted Surfaces, for Four European Locations." *International Journal of Solar Energy* 18 (4): 231–58. https://doi.org/10.1080/01425919708914321.

908 Qureshi, Jawed. 2022. "A Review of Fibre Reinforced Polymer Structures." *Fibers* 10 (3).
909 https://doi.org/10.3390/fib10030027.

910 Ribeiro, Filipe, Luís Correia, and José Sena-Cruz. 2024. "Hybridization in FRP Composites for Construction:
911 State-of-the-Art Review and Trends." *Journal of Composites for Construction* 28 (4).
912 https://doi.org/10.1061/jccof2.cceng-4486.

913 Saleem, Muhammad Azhar, Muhammad N. Zafar, Muhammad Mazhar Saleem, and Jun Xia. 2021. "Recent
914 Developments in the Prefabricated Bridge Deck Systems." *Case Studies in Construction Materials* 15
915 (December). https://doi.org/10.1016/j.cscm.2021.e00750.

916 Sanjuán, Miguel Ángel, Ángel Morales, and Aniceto Zaragoza. 2021. "Effect of Precast Concrete Pavement
917 Albedo on the Climate Change Mitigation in Spain." *Sustainability (Switzerland)* 13 (20).
918 https://doi.org/10.3390/su132011448.

919 Shahrooz, Bahram M, Andrew R Neumann, and Reiner M W Reising. 2007. "Durability of FRP Composite
920 Bridge Decks-Construction and Temperature Effects." *Int. J. Materials and Product Technology* 28 (1):
921 66–88. https://doi.org/10.1504/IJMPT.2007.011510.

922 Sharafi, P., S. Nemati, B. Samali, and M. Ghodrat. 2018. "Development of an Innovative Modular Foam-Filled
923 Panelized System for Rapidly Assembled Postdisaster Housing." *Buildings* 8 (8).
924 https://doi.org/10.3390/buildings8080097.

925 Shivalingaswamy, T, and B A Kagali. 2011. "Determination of the Declination of the Sun on a Given Day."
926 *European Journal of Physics Education* 3:1309–7202.

927 Silva, Tiago, Luís Correia, Mozhdeh Dehshirizadeh, and José Sena-Cruz. 2022. "Flexural Creep Response of
928 Hybrid GFRP–FRC Sandwich Panels." *Materials* 15 (7). https://doi.org/10.3390/ma15072536.

929 "Solar Position Algorithm (SPA)." n.d. Accessed May 20, 2024. https://midcdmz.nrel.gov/spa/.

930 Stankiewicz, B. 2017. "Durability of Glass Fiber-Reinforced Polymer Bridge Panel Based on Differential
931 Thermal Analysis, Dynamic Mechanical Analysis, and Differential Scanning Calorimetry Analysis."
932 *Journal of Composite Materials* 51 (16): 2301–13. https://doi.org/10.1177/0021998316669857.

933 Tang, Long. 2021. "Maintenance and Inspection of Fiber-Reinforced Polymer (FRP) Bridges: A Review of
934 Methods." *Materials* 14 (24). https://doi.org/10.3390/ma14247826.

935 Tayşi, Nildem, and Sallal Abid. 2015. "Temperature Distributions and Variations in Concrete Box-Girder
936 Bridges: Experimental and Finite Element Parametric Studies." *Advances in Structural Engineering* 18
937 (4): 469–86. https://doi.org/10.1260/1369-4332.18.4.469.

938 Thermo Fisher Scientific. 2011. "DT85M Series 3 Data Logger." https://www.thermofisher.com/.

939 Tuwair, Hesham, Jeffery Volz, Mohamed ElGawady, Mohaned Mohamed, K. Chandrashekhara, and Victor
940 Birman. 2016. "Behavior of GFRP Bridge Deck Panels Infilled with Polyurethane Foam under Various
941 Environmental Exposure." *Structures* 5 (February):141–51. https://doi.org/10.1016/j.istruc.2015.10.008.

942 Vizentin, Goran, and Goran Vukelic. 2021. "Failure Analysis of FRP Composites Exposed to Real Marine
943 Environment." In *Procedia Structural Integrity*, 37:233–40. Elsevier B.V.
944 https://doi.org/10.1016/j.prostr.2022.01.079.

945 "Weather Archive Guimarães - Meteoblue." n.d. Accessed May 22, 2024.
946 https://www.meteoblue.com/en/weather/historyclimate/weatherarchive/guimar%c3%a3es_portugal_27387
947 52?fcstlength=1m&year=2023&month=10.

948 Williams, G P. 1963. "Heat Transfer Coefficients for Natural Water Surfaces." *International Association of*
949 *Scientific Hydrology* 62:203–12.

950 Xi, Yunping, Sunyoung Chang, Andi Asiz, and Yue Li. 2004. "Long-Term Durability of Fiber-Reinforced
951 Polymers (FRPS) and in-Situ Monitoring of FRP Bridge Decks at O'Fallon Park Bridge." Denver.

952 Xia, Qi, Jian Zhang, Yongding Tian, and Yufeng Zhang. 2017. "Experimental Study of Thermal Effects on a
953 Long-Span Suspension Bridge." *Journal of Bridge Engineering* 22 (7).
954 https://doi.org/10.1061/(ASCE)BE.1943-5592.0001083.

955 Xia, Yong, Bo Chen, Xiao-qing Zhou, and You-lin Xu. 2013. "Field Monitoring and Numerical Analysis of
956 Tsing Ma Suspension Bridge Temperature Behavior." *Structural Control and Health Monitoring* 20 (4):
957 560–75. https://doi.org/10.1002/stc.515.

Xin, Haohui, Yuqing Liu, Ayman Mosallam, and Youyou Zhang. 2016. "Moisture Diffusion and Hygrothermal Aging of Pultruded Glass Fiber Reinforced Polymer Laminates in Bridge Application." *Composites Part B: Engineering* 100 (September):197–207. https://doi.org/10.1016/j.compositesb.2016.04.085.

Yang, Li Hua. 2014. "Research Status of FRP-Concrete Composite Beam/Bridge Deck Systems." *Applied Mechanics and Materials* 587–589:1424–29. https://doi.org/10.4028/www.scientific.net/AMM.587-589.1424.

Yousef, Bashria A.A., Ali Radwan, Abdul Ghani Olabi, and Mohammad Ali Abdelkareem. 2023. "Thermal Analysis of Solar Collectors." *Renewable Energy - Volume 1: Solar, Wind, and Hydropower Definitions, Developments, Applications, Case Studies, and Modelling and Simulation* 1 (January):93–119. https://doi.org/10.1016/B978-0-323-99568-9.00001-7.

Zhang, Hu, Wen Zhen Fang, Yue Ming Li, and Wen Quan Tao. 2017. "Experimental Study of the Thermal Conductivity of Polyurethane Foams." *Applied Thermal Engineering* 115:528–38. https://doi.org/10.1016/j.applthermaleng.2016.12.057.

Zhang, Lei, Yiqing Dai, Yu Bai, Wei Chen, and Jihong Ye. 2021. "Fire Performance of Loaded Fibre Reinforced Polymer Multicellular Composite Structures with Fire-Resistant Panels." *Construction and Building Materials* 296 (August). https://doi.org/10.1016/j.conbuildmat.2021.123733.

Zhou, Linren, Chunfang Liang, Lan Chen, and Yong Xia. 2017. "Numerical Simulation Method of Thermal Analysis for Bridges without Using Field Measurements." *Procedia Engineering* 210:240–45. https://doi.org/10.1016/j.proeng.2017.11.072.

TABLES

Table 1. Materials' properties summary.

Material	Density [kg/m^3]	Specific Heat [J/kg°C]	Thermal Conductivity [W/m°C]
SFRSCC	2420	900	1.55
GFRP	1890	1053	0.2495
PUR Foam	60	1450	0.03

LIST OF FIGURES

Fig. 1. GFRP hybrid sandwich panel: a) isometric view; b) cross-section at mid- length and sensors arrangement (units in mm).

Fig. 2. Initial experimental campaign: a) Phase I; b) Phase II; c) Phase III.

Fig. 3. Setups for the initial experimental campaign: a) Phase I; b) Phases II and III.

Fig. 4. Setup for the experimental campaign under external environmental conditions.

Fig. 5. Meshed numerical models for controlled climatic condition: a) front view; b) isometric view.

Fig. 6. Meshed numerical model for external climatic conditions.

Fig. 7. Global and diffuse solar radiation.

Fig. 8. Solar radiation on the lateral faces.

Fig. 9. Ground reflection irradiation.

Fig. 10. Air shade temperature and rainfall.

Fig. 11. Evaporative Heat Transfer Coefficient.

Fig. 12. Thermal profiles: a) Phase I; b) Phase II.

Fig. 13. Phase III – Sensors S1, S4 and S6: a) Overview; b) detail b; c) detail c; d) thermal profiles (all sensors).

Fig. 14. Experimental vs. numerical results: a) sensor S1; b) sensor S2; c) sensor S3; d) sensor S4;

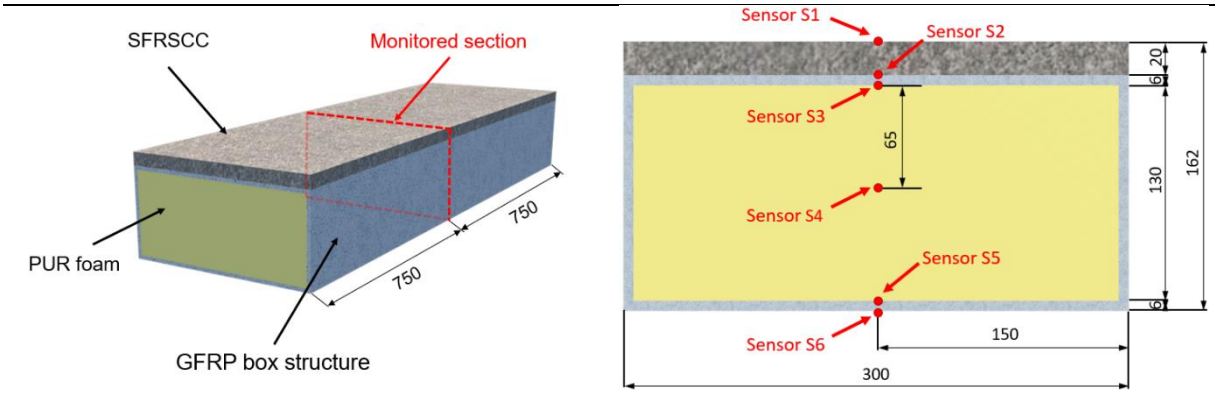
Fig. 15. Thermal profiles for the external environment experimental campaign.

Fig. 16. Air shade temperature in the most severe cases for Guimarães: a) week with the highest temperature; b) week with the lowest temperature.

Fig. 17. Solar radiation in the most severe cases for Guimarães: a) week with the highest temperature; b) week with the lowest temperature.

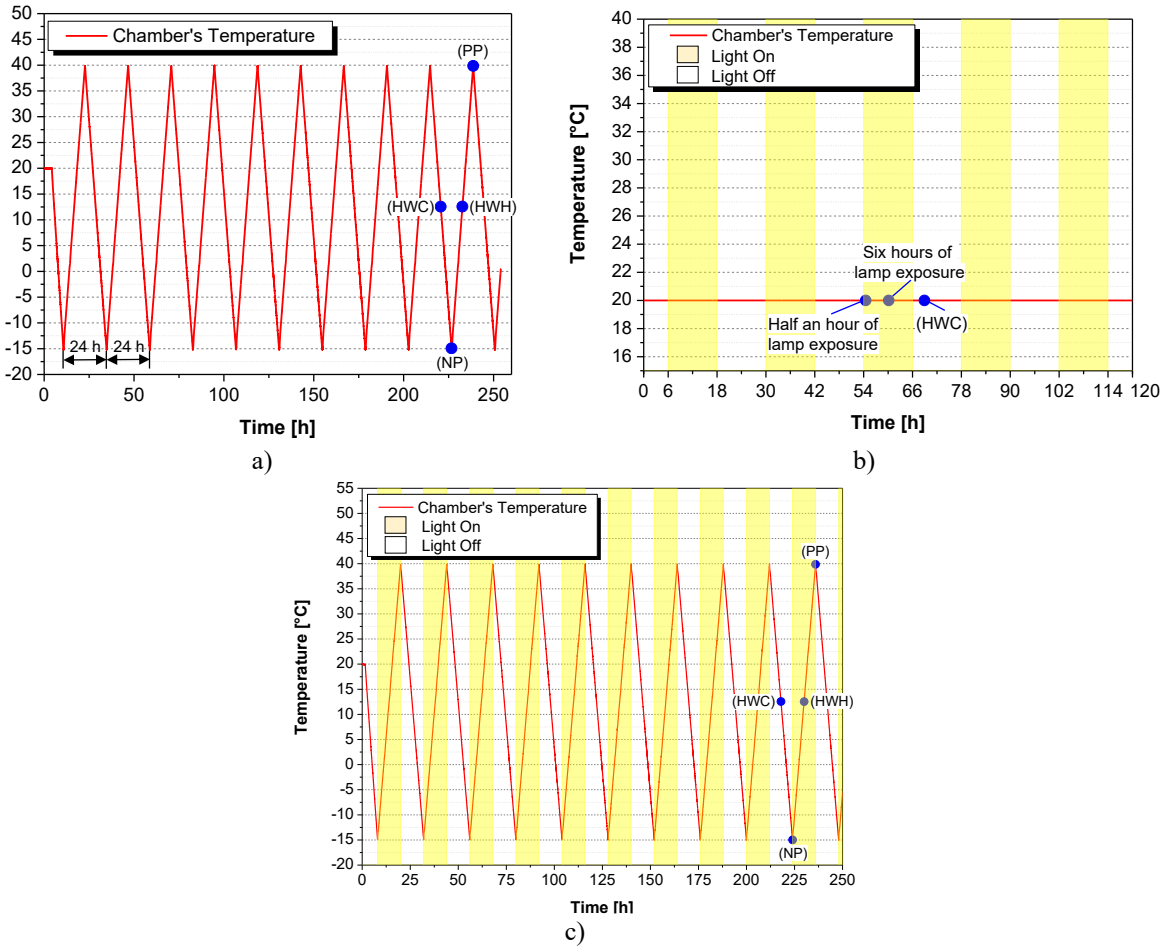
Fig. 18. Ground reflection radiation in the most severe cases for Guimarães: a) week with the highest temperature; b) week with the lowest temperature.

Fig. 19. Thermal distribution in the most severe cases for Guimarães: a) highest temperature peak; b) lowest temperature peak.



a) b)

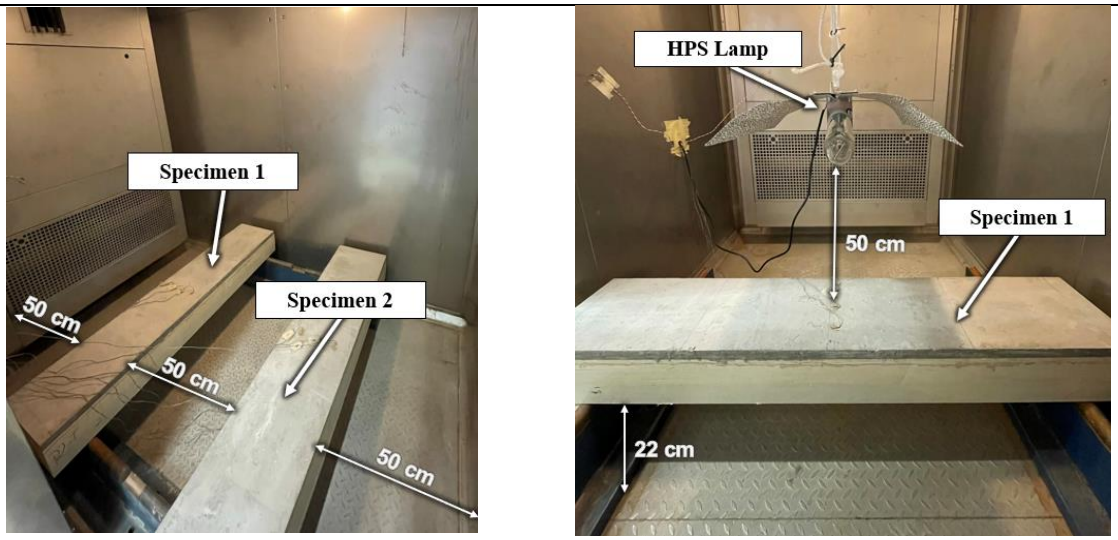
Figure 1 - GFRP hybrid sandwich panel: a) isometric view; b) cross-section at mid- length and sensors arrangement (units in mm).



a) b)

c)

Figure 2 - Initial experimental campaign: a) Phase I; b) Phase II; c) Phase III.



a) b)

Figure 3 - Setups for the initial experimental campaign: a) Phase I; b) Phases II and III.

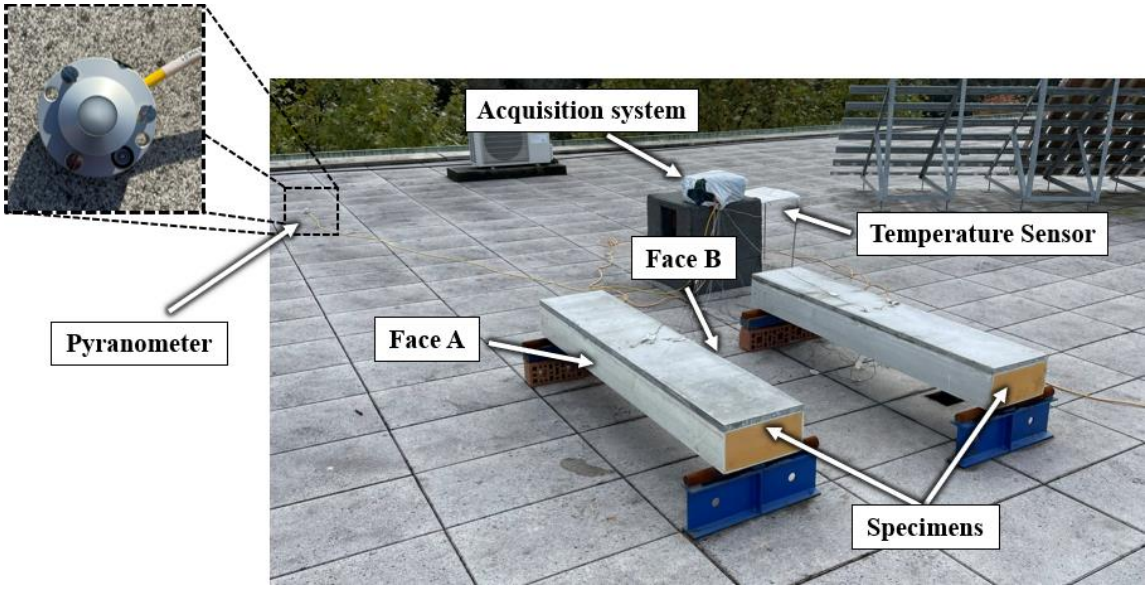
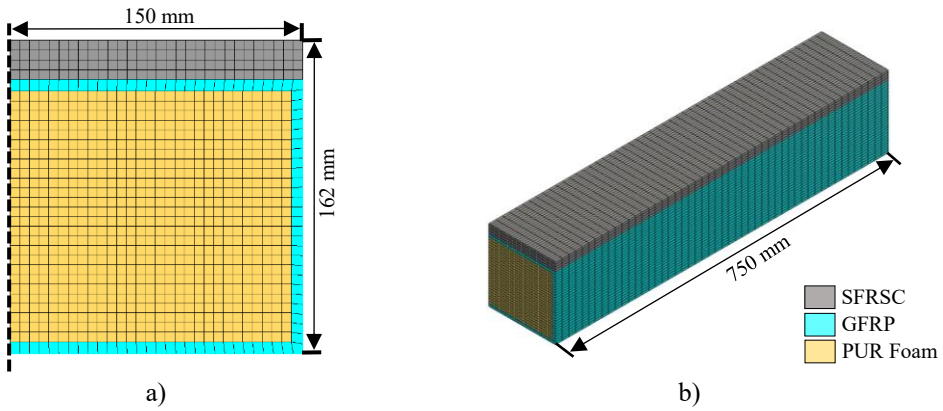
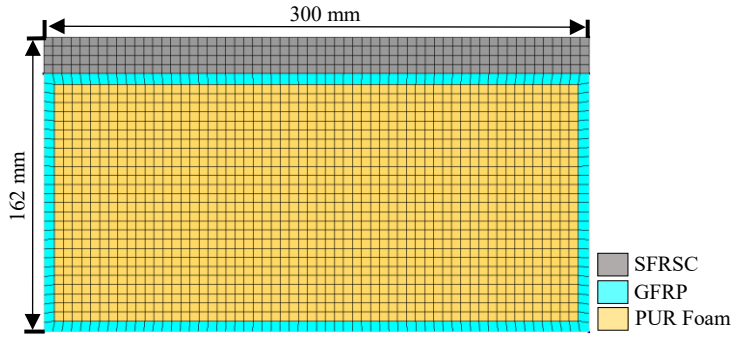


Figure 4 - Setup for the experimental campaign under external environmental conditions.



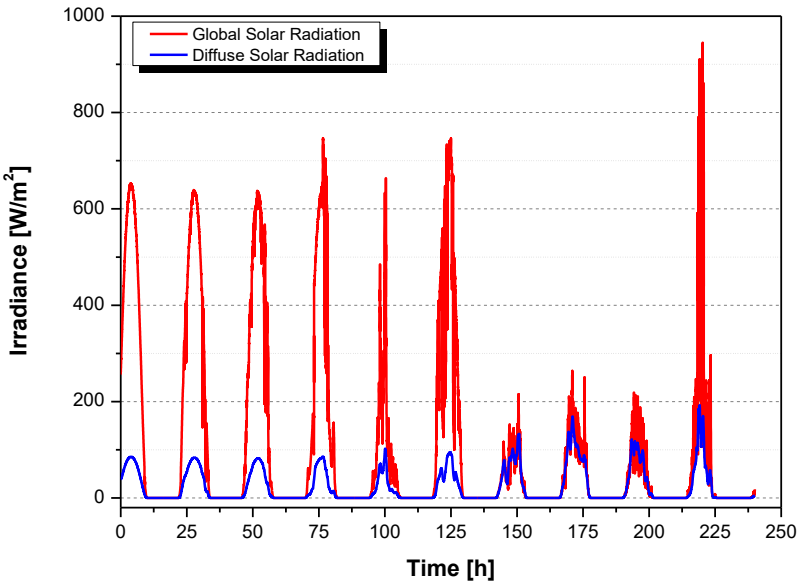
1018 *Figure 5 - Meshed numerical models for controlled climatic condition: a) front view; b) isometric view.*

1019



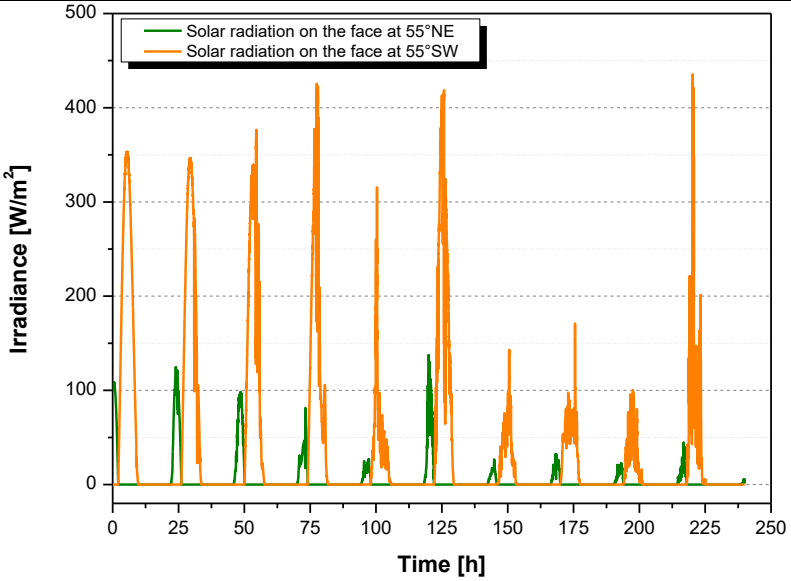
1020 *Figure 6 - Meshed numerical model for external climatic conditions.*

1021



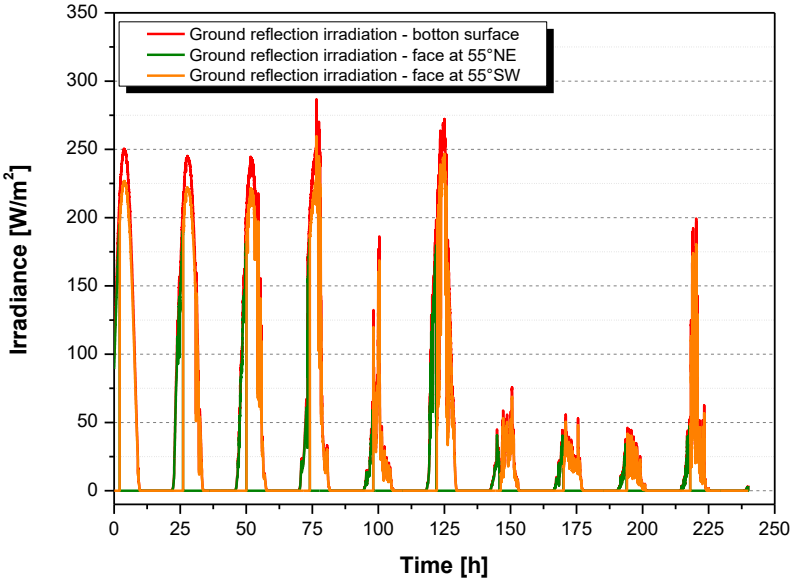
1022

1023 *Figure 7 - Global and diffuse solar radiation.*



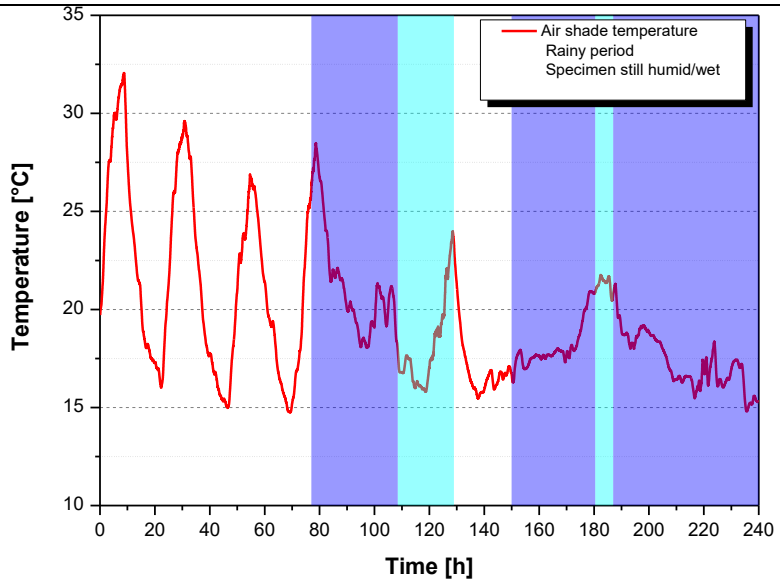
1024

1025 *Figure 8 - Solar radiation on the lateral faces.*



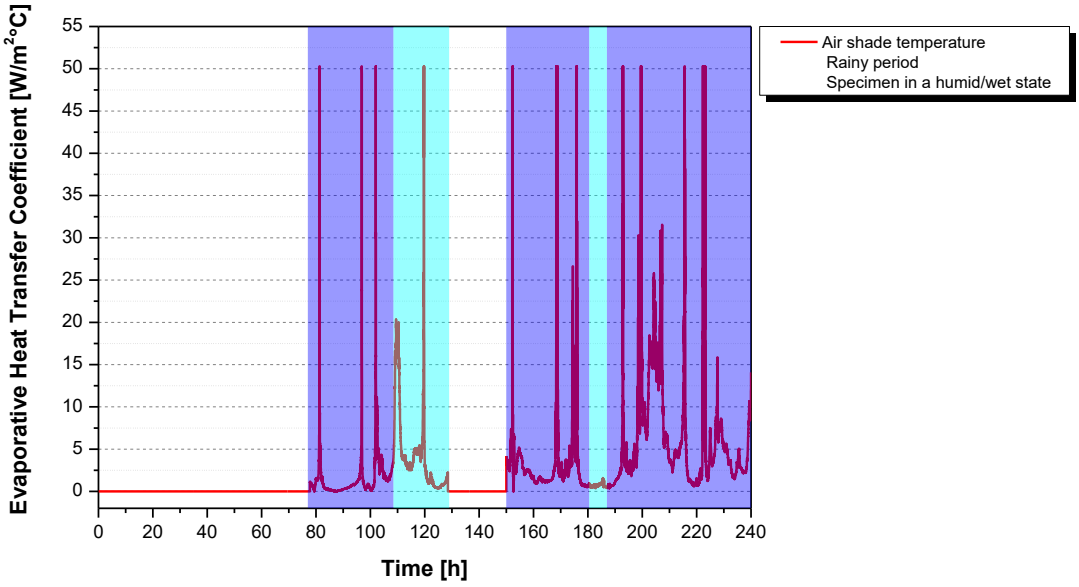
1026

1027 *Figure 9 - Ground reflection irradiation.*



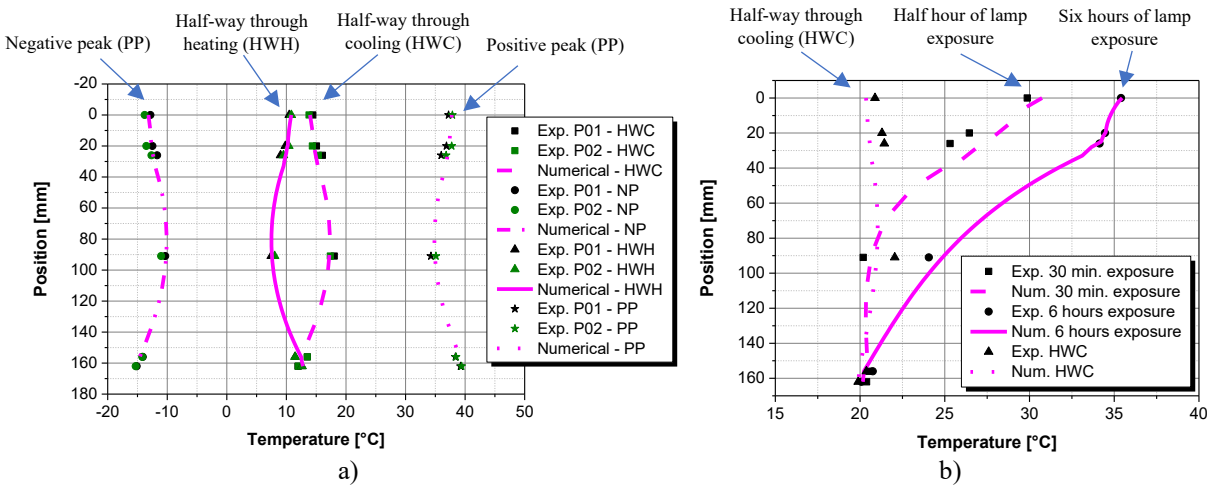
1028

1029 *Figure 10 - Air shade temperature and rainfall.*

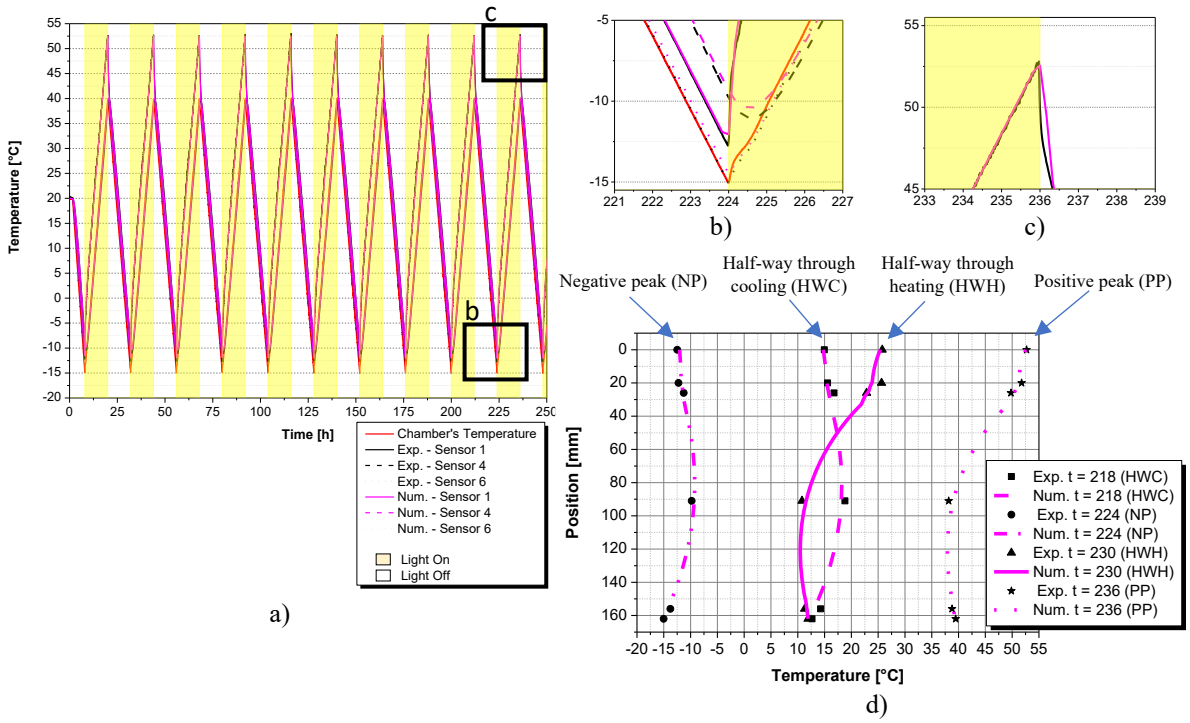


1030

1031 *Figure 11 - Evaporative Heat Transfer Coefficient.*



1032 *Figure 12 - Thermal profiles: a) Phase I; b) Phase II.*



1033 *Figure 13 - Phase III – Sensors S1, S4 and S6: a) Overview; b) detail b; c) detail c; d) thermal profiles (all*

1034 *sensors).*

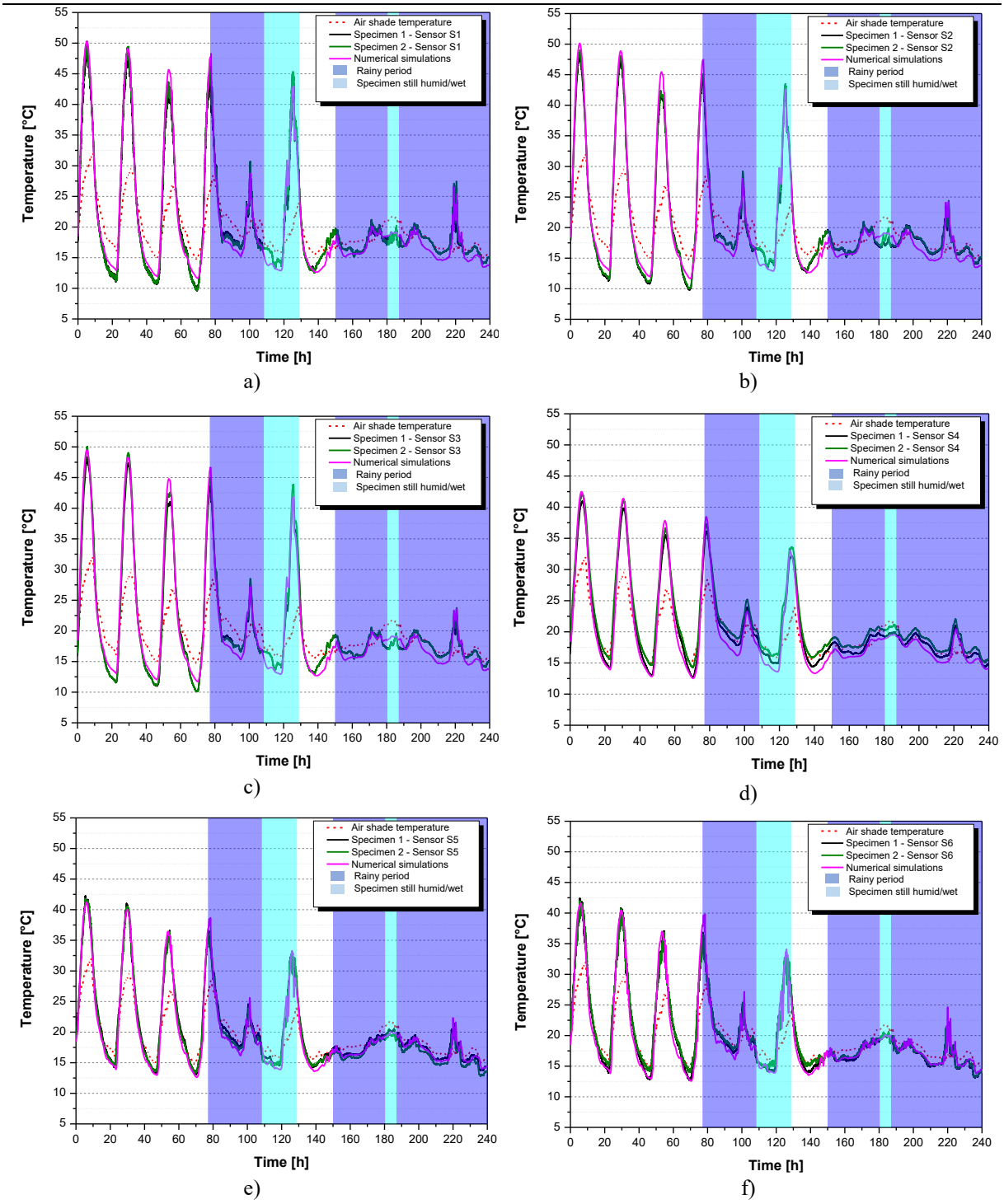


Figure 14 - Experimental vs. numerical results: a) sensor S1; b) sensor S2; c) sensor S3; d) sensor S4; e) sensor S5; f) sensor S6. (see also Figure b).

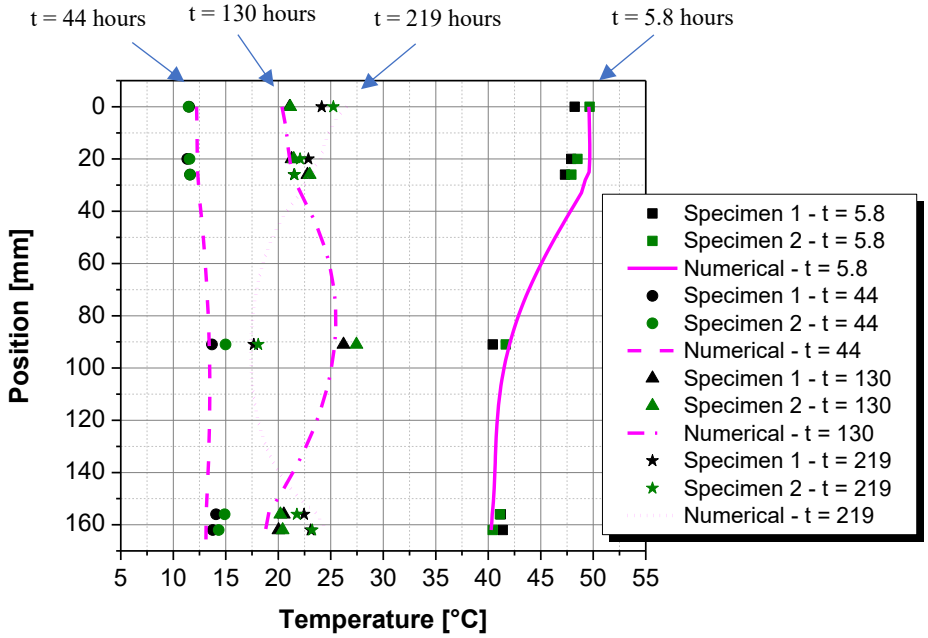


Figure 15 - Thermal profiles for the external environment experimental campaign.

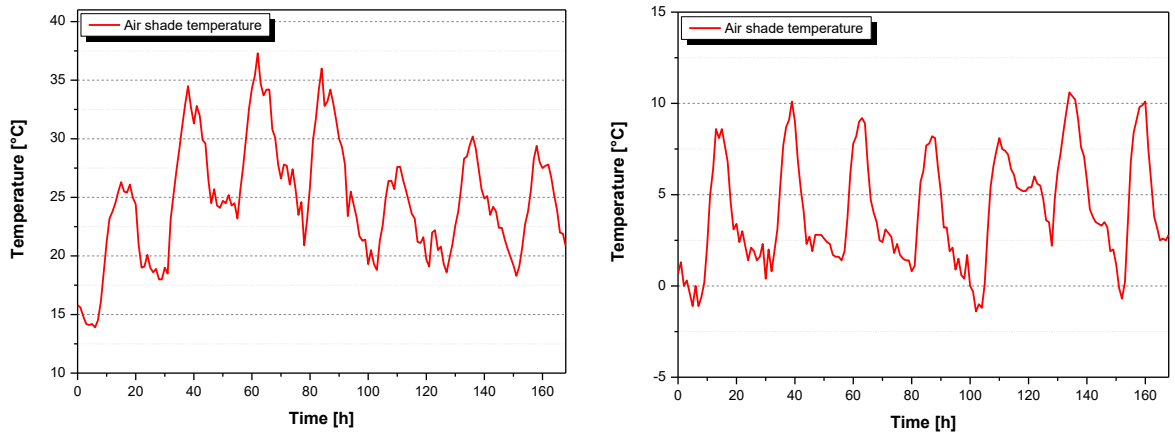
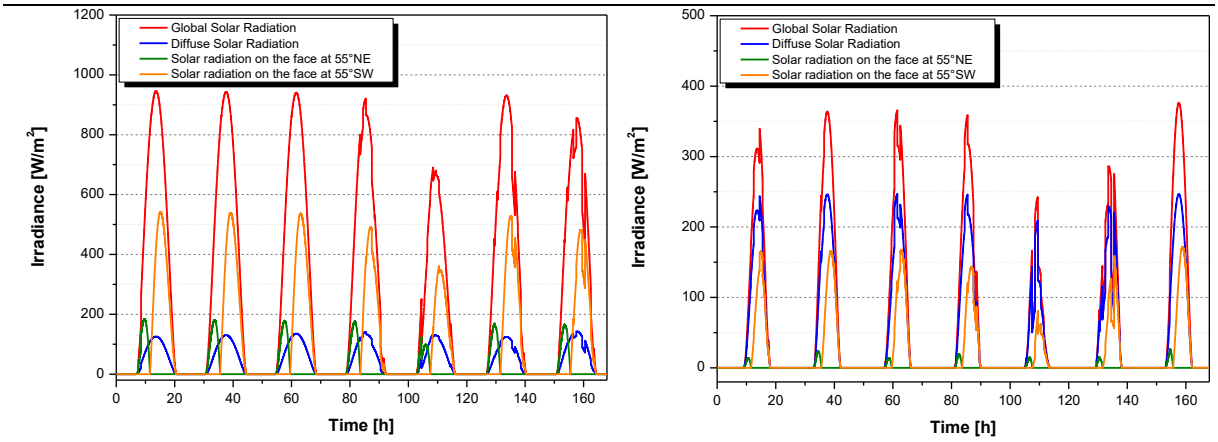
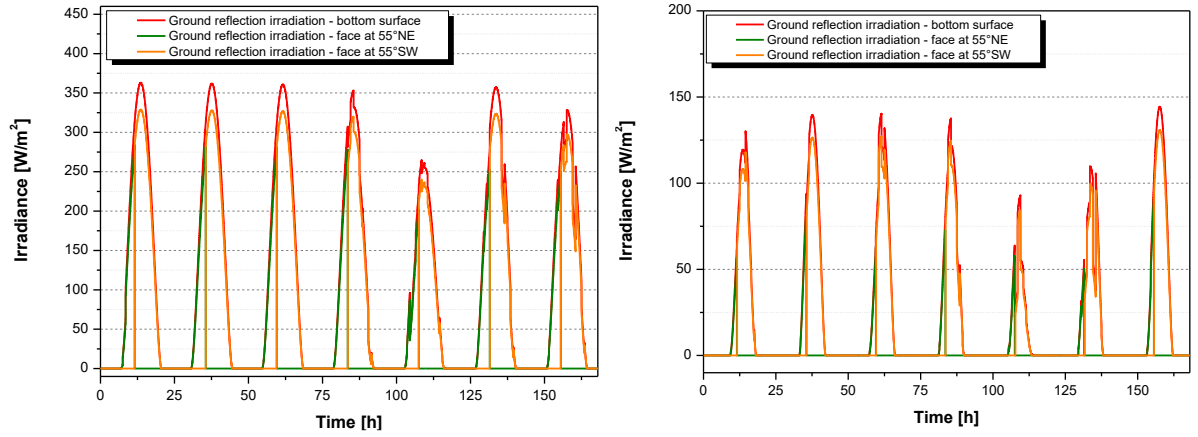


Figure 16 - Air shade temperature in the most severe cases for Guimarães: a) week with the highest temperature; b) week with the lowest temperature.



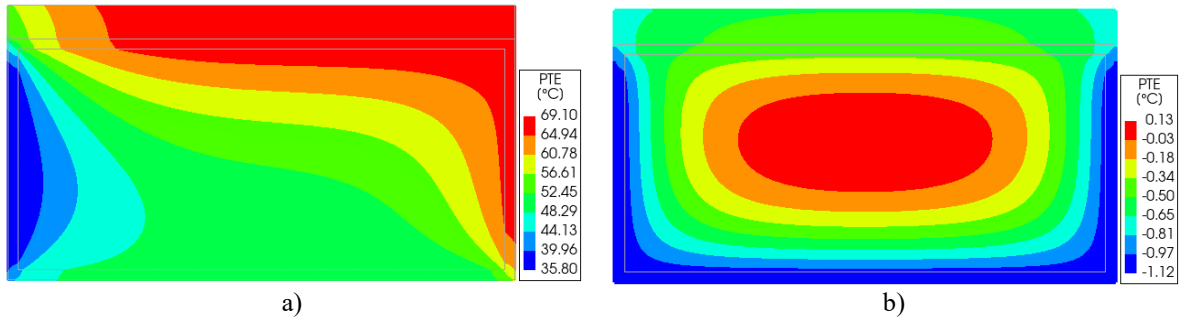
1042 *Figure 17 - Solar radiation in the most severe cases for Guimarães: a) week with the highest temperature;*

1043 *b) week with the lowest temperature.*



1044 *Figure 18 - Ground reflection radiation in the most severe cases for Guimarães: a) week with the highest*

1045 *temperature; b) week with the lowest temperature.*



1046 *Figure 19 - Thermal distribution in the most severe cases for Guimarães: a) highest temperature peak; b) lowest*

1047 *temperature peak.*

1048